Comparative wear behaviour of advanced tool materials in milling compacted graphite iron
-CGI450 vs SSF CGI350

Yuxinyue Liu

2026

MASTER THESIS
DIVISION OF PRODUCTION AND MATERIALS ENGINEERING
LUND UNIVERSITY

Supervisor: Christina Windmark
Co Supervisor: Juan Manuel Bello Bermejo
Co Supervisor: Joakim Sandberg
Examiner: Oleksandr Gutnichenko

Author: Yuxinyue Liu
Lund, Sweden 2026

Avdelningen för Industriell Produktion
Lunds Tekniska Högskola
Lunds universitet
Box 118
221 00 Lund
Sverige

Division of Production and Materials Engineering
LTH, Faculty of Engineering
Lund University
Box 118
SE-221 00 Lund
Sweden

Printed in Sweden
Media-Tryck
Lund University

Foreword

This master's thesis represents the culmination of my studies in Production and Materials Engineering at Lund University. The work has provided an opportunity to apply and expand the knowledge gained throughout the programme, while also developing a deeper understanding of manufacturing processes, metal cutting, and scientific research.

I would first like to express my sincere gratitude to my supervisor, Christina Windmark, for her invaluable guidance, encouragement, and continuous support throughout this project. My deep appreciation also extends to my co-supervisors, Juan Manuel Bello Bermejo and Joakim Sandberg, for generously sharing their expertise and providing insightful discussions during both the experimental and analytical phases. Their knowledge and advice were essential in completing this work.

Furthermore, I would like to thank my examiner, Oleksandr Gutnichenko, for his time and evaluation of this thesis. I am also grateful to the staff and colleagues at the Division of Production and Materials Engineering for their assistance during the experimental work and for creating a supportive and inspiring research environment.

Finally, I would like to thank my family and friends for their encouragement and support throughout my studies. Their unwavering support has been a constant source of motivation throughout my time at Lund University.

Lund 2026-05-28

Yuxinyue Liu

Abstract

This thesis investigates the wear behaviour of advanced cutting tools during the milling of fully pearlitic CGI 450 and ferritic-pearlitic SSF CGI 350. The hard CGI 450 primarily induced mechanical abrasive wear, whereas the highly ductile, ferrite-rich SSF CGI 350 triggered adhesive wear and built-up edge formation. EDS analysis confirmed the dynamic formation of a protective Mg-Si-O layer, which extended tool life under extreme loads. For tool life modelling, a Colding tool life model implemented in python achieved expected statistical accuracy. However, mathematical singularities emerged in the modelling results. These anomalies serve as mathematical proof of the micro-scale chemical interference, demonstrating that traditional empirical models become physically unstable under chemical interactions. This indicates that optimal machining of advanced cast irons requires tool selection strategies that balance mechanical abrasion resistance with chemical compatibility.

Keywords: Milling, Tool life, Graphite Iron, Colding Model.

Table of Content

List of Abbreviations

Symbol/ Abbreviation	Designation/definition (unit)
a_e	Radial depth of cut (mm)
a_p	Axial depth of cut (mm)
n	Spindle speed (rpm)
f_z	Feed per tooth (mm)
DCx	Maximum cutting diameter (mm)
DC	Minimum cutting diameter (mm)
DCw	Working (Effective) cutting diameter(mm)
T	Tool life (s)
l_{pass}	Pass length (mm)
l_{arc}	Arc length (mm)
l_w	Length of pass(mm)
v_c	Cutting speed (m/min)
v_f	Table feed / Feed Speed (mm/min)
$v_{c,exp}$	The experimental cutting speed(mm/min)
$v_{c,mod}$	The modeled cutting speed(mm/min)
z	Number of effective teeth (pcs)
h_e	Equivalent chip thickness (μm)
$f_{speed_{CC}}$	Feed speed(mm/min)
$passes_{CC}$	Number of passes
r_ε	Nose radius(mm)
d_{DC}	Tool diameter(mm)
Jay	Scaling constant

1. Introduction

1.1. Background

Milling is one of the most fundamental and widely used machining processes in the modern manufacturing industry. In recent years, the metal cutting industry has continuously sought materials that offer higher strength-to-weight ratios to reduce emissions and improve performance. Compacted Graphite Iron (CGI) has emerged as a premier choice for manufacturing engine blocks and cylinder heads due to its excellent mechanical properties, which lie between those of grey cast iron and ductile cast iron[1].

However, the superior strength and thermal properties of CGI come with a trade-off: poor machinability. Compared to traditional grey cast iron, machining CGI generates higher cutting forces and temperatures, leading to accelerated deterioration of cutting tools[1]. Cemented carbide tools are currently the industry standard for machining CGI[1]. Yet, rapid and unpredictable tool wear (such as flank wear) directly compromises the dimensional accuracy and surface integrity of the machined workpiece. Unplanned tool changes not only cause production downtime but also significantly increase manufacturing costs[2]. Therefore, accurately monitoring and predicting the tool wear state and tool life during the milling of CGI is of paramount importance for optimizing cutting parameters, ensuring work piece quality, and reducing overall production costs[3].

1.2. Previous research

Predicting tool life accurately is a cornerstone of optimizing metal cutting processes. Historically, the extended Taylor's tool life equation[4] has been the most commonly used empirical model. While widely applicable, it often falls short in accurately capturing the complex, non-linear relationships between cutting speed, equivalent chip thickness, and tool life across a broad range of cutting data[3].

To address these limitations, the Colding tool life model was developed[5], which provides a much more comprehensive and accurate representation of machinability by integrating the concept of equivalent chip thickness. However, the practical application of the Colding model has historically been hindered by the mathematical complexity of determining its five constants. Recently, a systematic approach for evaluating these parameters was presented in the study Optimal modelling of Colding parameters for round inserts with respect to tool use-time criteria[3]. This research established an optimization-based methodology to accurately determine the constants, allowing for the generation of precise tool life curves.

Building upon these advanced modelling techniques, recent research has begun to address the specific challenges of machining difficult-to-cut materials like CGI. For instance, the recent thesis Tool Life Prediction of Cemented Carbide Tools During Milling of Compacted Graphite Iron successfully applied these theoretical frameworks to the milling of CGI[6]. The study demonstrated the feasibility of utilizing advanced predictive models to accurately map the wear behaviour and predict the tool life of cemented carbide tools when subjected to the severe thermo-mechanical loads' characteristic of CGI milling.

While previous studies have successfully established robust mathematical models for predicting tool wear and tool life during CGI milling, the research has predominantly focused on the tool itself. There remains a noticeable gap in directly and quantitatively linking these advanced tool life models (such as the optimized Colding model) to the continuous deterioration of the workpiece material properties. To achieve a truly optimized manufacturing process, it is essential not only to predict when the tool will fail but also to understand how the progressive tool wear dynamically impacts the surface integrity and dimensional accuracy of the CGI workpiece.

1.3. Aim

The primary aim of this thesis is to investigate and quantitatively model the complex tool wear mechanisms and tool life behaviours when milling cast irons using diverse cutting tool materials. By bridging the gap between macroscopic mathematical tool life prediction and microscopic interfacial phenomena, this research seeks to provide a understanding of how non-linear tool deterioration dynamically impacts the overall machinability and workpiece integrity.

2. Theoretical background

2.1. Workpiece material: Compacted Graphite Iron

Compacted graphite iron offers a highly advantageous performance-to-cost balance for heavy-duty automotive components, such as engine blocks, cylinder heads, and piston rings[7]. Microstructurally, CGI is characterized by vermicular (worm-like) graphite particles embedded within a metallic matrix. This unique graphite morphology positions the material characteristics of CGI strictly between those of highly ductile nodular cast iron and highly thermally conductive grey cast iron. In terms of mechanical properties, CGI possesses greater tensile and fatigue strength than grey cast iron, alongside better thermal conductivity and damping capacity compared to nodular cast iron[8].

Despite these enhanced material properties, the superior strength and thermal characteristics of CGI come with a significant trade-off: inherently poor machinability. Machining CGI generates substantially higher cutting forces and temperatures compared to traditional grey cast iron, leading to rapid and unpredictable tool degradation. This accelerated wear remains a primary bottleneck for manufacturing productivity and surface integrity. To systematically understand this tool degradation, it is critical to evaluate how specific microstructural variations within CGI grades dictate different wear responses[7].

2.1.1. CGI450

CGI 450 serves as the high-strength reference material in this study. Its microstructure is dominated by a fully pearlitic matrix, which is intentionally engineered to fulfill stringent static strength requirements. However, this fully pearlitic structure makes it highly abrasive during machining. When milling CGI 450, the extreme hardness of the pearlite colonies induces severe thermo-mechanical loads at the tool-chip interface, typically driving aggressive mechanical wear (such as rapid flank wear and comb cracking). Consequently, industry guidelines generally recommend that cutting speeds for CGI 450 should be reduced to approximately 75% of the speeds typically used for grey cast iron to prevent catastrophic tool failure[7].

2.1.2. SSF CGI 350

In contrast to the fully pearlitic reference grade, Solution Strengthened Ferritic (SSF) CGI 350 represents a softer alternative CGI grade. It features a mixed ferritic–pearlitic matrix. The introduction of a higher ferrite fraction fundamentally alters its machinability profile.

To understand this shift, it is essential to examine the fundamental micromechanical interactions within a mixed microstructure under load. Mechanical microcracking and failure predominantly initiate within the harder and more brittle pearlite colonies[9]. Specifically, this failure occurs through the fracture of cementite lamellae. These microcracks propagate rapidly through the pearlite. However, they stop when they encounter the boundaries of the softer ferrite grains. The high plastic deformation capacity of the ferrite effectively blocks the crack propagation.

Therefore, a higher ferrite fraction in SSF CGI 350 means the material contains fewer pearlite colonies to initiate hard fracture. This microstructural shift reduces the overall bulk hardness. It potentially lowers the purely abrasive wear on the cutting tool. However, this shift significantly increases the ductility of the bulk matrix. From a tribological perspective, this softer and highly ductile matrix increases the material's susceptibility to severe plastic deformation in the cutting zone.

2.2. Cutting tool material

2.2.1. Ceramic

To meet the demands of high-speed machining, ceramic cutting tools are frequently employed due to their hot hardness and chemical stability at elevated temperatures. According to Ståhl[7], ceramic materials maintain their hardness and resist oxidation much better than conventional cemented carbides, making them highly suitable for generating high cutting speeds without suffering from immediate thermal softening.

However, the primary limitation of standard oxide ceramics is their inherent brittleness, characterized by low fracture toughness and poor thermal shock resistance[7]. To counter this, modern machining operations often utilize mixed ceramics or Sialon (Silicon-Aluminum-Oxynitride). Sialon ceramics, in particular, exhibit significantly higher toughness and thermal shock resistance, which makes them highly effective for the continuous and semi-interrupted cutting of cast irons. Despite these improvements, ceramic tools generally require highly rigid machine setups and are predominantly used in dry machining conditions to prevent the initiation of thermal fatigue cracks caused by rapid temperature fluctuations.

2.2.2. Cemented Carbide

Cemented carbides (CC) are powder-metallurgically manufactured composite materials that are widely used in metal cutting due to their high wear resistance, high hardness, and strength[7].

The primary composition and structural characteristics of cemented carbide tools include:

- They consist of hard particles sintered together by a tough binding metal, with tungsten carbide (WC) being the most important hard phase and cobalt being the most commonly employed binder.
- Most cemented carbides used for cutting tools are composed of 80 to 95 volume percent of hard particles, while the remainder is cobalt.
- The carbide particles typically have a grain size ranging from 0.5 to 4 μm, forming partly interconnected skeletons.
- The characteristics of the final tool are primarily dictated by the composition of the carbides, the grain size of the particles, and the binder content.

2.2.3. Cubic boron nitride

Cubic Boron Nitride (cBN) is an advanced superhard tool material, second only to diamond in terms of absolute hardness[7]. The cBN tools have high hot hardness, high thermal conductivity, and a low coefficient of thermal expansion. These characteristics make cBN an outstanding choice for high-speed machining and hard part machining of ferrous alloys[7].

When machining cast irons, the microstructural composition of the workpiece is the critical determining factor for the success of cBN tools. cBN performs exceptionally well when machining abrasive, pearlitic, or martensitic structures[7].

But there is a fundamental limitation of cBN which is its chemical affinity with pure ferrite at high temperatures. During the high-speed cutting process, the elevated temperatures at the cutting zone trigger a chemical reaction between the cBN tool material and the ferritic phases in the workpiece, leading to rapid and severe chemical wear[10].

2.3. The milling process

Milling represents a highly dynamic and complex machining operation utilizing a rotating multi-point cutter. The fundamental aspect distinguishing milling from continuous cutting operations, such as turning, is its inherently interrupted cutting nature[7]. As the cutter rotates, each individual cutting insert undergoes a periodic engagement cycle, repeatedly entering and exiting the workpiece material. This cyclical engagement subjects the cutting edge to severe mechanical shocks and transient thermal gradients.

During the entry phase of each revolution, the cutting edge experiences a rapid escalation of mechanical impact stress and localized temperature. Upon exiting the cutting zone, the edge undergoes abrupt unloading and rapid cooling, either through exposure to the ambient environment or the application of cutting fluid. This cyclic thermal loading creates steep temperature gradients within the tool material, inducing alternating compressive and tensile thermal stresses. Over extended machining periods, this thermal fatigue leads to the nucleation and propagation of thermal cracks perpendicular to the cutting edge. These defects are frequently referred to as comb cracks[7].

Furthermore, the kinematics of the milling process dictate that the undeformed chip thickness varies continuously throughout the engagement arc. This continuously changing chip geometry complicates the direct evaluation of cutting forces and tool life. To resolve this and normalize the varying thermo-mechanical loads into a singular, representative mathematical variable, Swedish cutting theory widely utilizes the concept of equivalent chip thickness, originally formulated by Woxén and later extensively expanded for multi-axis tool life modelling by Colding[11]. The equivalent chip thickness mathematically integrates the chip cross-sectional area over the active cutting edge contact length, providing a vital baseline parameter for macroscopic tool life equations in interrupted cutting regimes.

2.4. Tool wear

Tool degradation during metal cutting is a complex, multi-faceted phenomenon. To fully comprehend tool failure, it is essential to distinguish between the macroscopic geometric forms of wear observed on the tool, and the underlying microscopic mechanisms that drive them[7]. The synergistic combination of these tribological processes ultimately dictates the tool life and performance.

2.4.1. Common forms of tool wear

Macroscopically, tool wear is typically classified by its geometric location and phenomenological appearance. In the machining of advanced cast irons, the two most predominant forms are:

2.4.1.1. Flank wear

This is the most common and predictable form of wear, occurring on the clearance face (flank) of the cutting tool. It is primarily driven by the intense frictional rubbing between the tool flank and the newly machined workpiece surface. As flank wear progresses, the contact area increases, leading to higher cutting forces and elevated temperatures. It is generally evaluated by measuring the average wear land width[11].

2.4.1.2. Crater wear

Unlike flank wear, crater wear manifests as a concave depression on the rake face of the tool. It occurs in the region where the high-temperature, high-velocity chip intimately contacts and slides over the tool surface. Excessive crater wear structurally weakens the cutting edge, drastically increasing the risk of sudden edge breakage or catastrophic plastic deformation[12].

2.4.2. Tool wear mechanisms

While flank and crater wear describe where the wear happens, the actual material removal is governed by a combination of physical and chemical mechanisms operating at the tool-chip interface.

2.4.2.1. Abrasive wear

Abrasive wear is a primarily mechanical degradation process driven by hard micro-constituents embedded within the workpiece matrix. The workpiece microstructure contains various hard phases, including cementite lamellae within pearlite colonies and intercellular carbides. When these hard phases slide across the tool surface, they act as micro-plows that physically scratch and remove tool material particles[12]. In the machining of compacted graphite iron, the highly abrasive nature of the pearlitic matrix accelerates this mechanical scouring, serving as the primary driver for steady-state flank wear.

2.4.2.2. Adhesive wear

Adhesive wear arises from the extreme localized contact pressures generated at the intimate contact zones of the tool-chip interface. Solid-state micro-welds form between the flowing chip and the tool surface, which are subsequently forcefully sheared by the relative motion. Adhesive wear is particularly pronounced when machining highly ductile materials such as solid-solution strengthened ferritic iron. The severe plastic deformation promotes continuous material adhesion, often culminating in the formation of a Built-Up Edge (BUE) or Built-Up Layer (BUL)[13]. The periodic formation and detachment of these structures induce cyclic tearing, directly contributing to micro-chipping.

2.4.2.3. Chemical wear

As cutting speeds increase, localized temperatures at the tool-chip interface can easily exceed to the point where thermally activated wear mechanisms begin to dominate[14]. High temperatures catalyze diffusion processes, which are the cause of crater wear on the rake face.

Concurrently, environmental oxygen and reactive elements within the tool-workpiece system trigger complex chemical reactions. Under specific thermodynamic thresholds, trace elements originating from the workpiece interact dynamically with the oxidized elements of the tool surface or coating. This interfacial interaction can lead to the dynamic in-situ formation of highly dense[14]. While classified as a chemical reaction product, such layer can temporarily act as an effective thermal barrier and solid lubricant, inducing highly non-linear tool life behaviours.

2.4.2.4. Thermal fatigue

Due to the cyclic thermal shocking inherent to the milling process[7], the tool surface undergoes high-frequency alternating thermal expansion and contraction. This generates alternating thermal stress fields, which inevitably initiate networks of microscopic thermal fatigue cracks (comb cracks), ultimately leading to structural fracture[7].

3. Methodology

3.1. Experimental Setup

To evaluate the machinability differences and tool wear mechanisms, a series of face milling experiments were conducted. The experimental setup was designed to isolate the effects of workpiece microstructure and cutting tool material on tool life and wear progression.

3.1.1. Workpiece Materials

The face milling tests were performed on 2 distinct grades of CGI to provide a comparative analysis of their machinability and wear mechanisms:

CGI 450 (Pearlitic Grade): A high-strength CGI grade (EN-GJV-450) characterized by a predominantly pearlitic matrix. This grade offers high hardness and tensile strength (minimum 450 MPa UTS) but relatively lower ductility. It represents the conventional standard for demanding structural applications under high thermal and mechanical loads, such as heavy-duty engine cylinder heads.

SSF CGI 350 (Ferritic Grade): A Solution-Strengthened Ferritic CGI grade (EN-GJV-350). In contrast to CGI 450, this grade possesses a solid-solution strengthened, predominantly ferritic matrix. This unique microstructure provides superior ductility, toughness, and thermal conductivity. However, it significantly alters the machining behaviour, making the material softer and inherently more adhesive ("gummier") during cutting operations.

3.1.2. Machine Tool and Machining Parameters

All machining operations were executed on a Bridgeport XR 1270 CNC Milling Center. The cutting parameters were established as follows:

Axial depth of cut (a_p): 2.0 mm.

Radial depth of cut (a_e): 40 mm.

Cutting diameter (D_c): D_c varied depending on the specific toolholder configuration (63 mm and 80 mm).

The primary variables adjusted during the testing matrix were the cutting speed and the feed per tooth, which were systematically varied to formulate the Colding tool life models for the respective tool-workpiece combinations.

3.1.3. Cutting tools

To eliminate the influence of multi-insert variations and isolate the wear performance of a single cutting edge, only one insert was actively engaged during the tests (effective number of teeth, z = 1).

For each cutting tool material, the specific configurations and machine attachments are detailed below.

3.1.3.1. The ceramic tools

Toolholder: R200-068Q27-12M. This toolholder is a high-performance face milling cutter body designed for round inserts. Based on the manufacturer's specifications[15], this cutter body features an cutting diameter of 68 mm, a 27 mm arbor connection, a 0° entering angle, and an internal axial concentric coolant system. While designed with six insert seats, in this study it was configured with a single active insert to track individual edge wear.

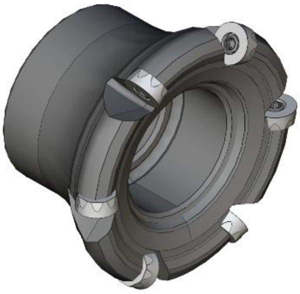

Figure 1: *Sandvik Coromant R200-068Q27-12M Toolholder*

Inserts: RCKT 12 04 MO 6190. According to the manufacturer's specifications[16], this is an uncoated ceramic round insert. Its geometrical characteristics include an inscribed circle diameter of 12 mm, a thickness of 4.76 mm, and a 7° major clearance angle designed to minimize flank friction.

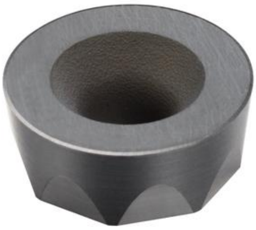

Figure 2: *Sandvik Coromant RCKT 12 04 MO 6190 Insert*

Machine attachment: A1B05-40 27 035. Serving as the interface between the machine spindle and the cutter body, this arbor features a standard DIN 69871 form AD/B (size 40) machine-side taper and a 27 mm connection that matches the toolholder[17]. Also, it supports an internal coolant delivery system with both axial concentric and radial entry capabilities.

Figure 3: *Sandvik Coromant A1B05-40 27 035 adaptor*

3.1.3.2. The CC tools

Toolholoder: R220.29I-0080-06.6A. From the manufacturer's specifications[18], this face milling cutter body features a cutting diameter of 80 mm, a standard 27 mm arbor connection, a 0° entering angle, and an internal axial concentric coolant system. Similar to the ceramic tooling setup, although it is engineered with six peripheral insert seats, it was configured with a single active insert to isolate and track individual edge wear.

Figure 4: *Seco R220. 29I-0080-06.6A Toolholder*

Insert: RPKW1204M0T6-MD10, MK2050. According to the manufacturer's specifications[19], this is a PVD-coated carbide round insert. Its geometrical features include an insert diameter of 12.00 mm, a thickness of 4.76 mm, a

0° insert rake angle, and an 11° major clearance angle designed for specific flank clearance requirements.

Figure 5: *Seco RPKW1204M0T6-MD10, MK2050 Insert*

Machine attachment: A1B05-40 27 035. The machine attachment used for CC machining was identical to the one used for the ceramic tools.

3.1.3.3. The cBN tools

Toolhodler: R220.70-0063-09-6. According to the manufacturer's specifications[20], this face milling cutter body features a cutting diameter of 63 mm and a 22 mm arbor connection bore. Consistent with the overall experimental methodology, although designed with six peripheral insert seats, it was configured with a single insert to isolate the wear mechanics.

Figure 6: *Seco R220.70-0063-09-6 Toolholder*

Insert: RNMN120300S CBN300. From the manufacturer's specifications[21], this is a PcBN round insert. Its geometrical characteristics include an insert diameter of 12.70 mm and a thickness of 3.18 mm. Featuring a geometry with a 0° clearance angle, it is engineered to provide maximum cutting edge strength under extreme mechanical loads.

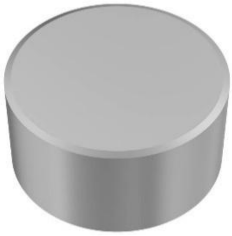

Figure 7: *Seco RNMN120300S CBN300 Insert*

Machine attachment: DIN40ADB-SM22-035-L1. As an interface between the machine spindle and the cutter body, this arbor features a DIN 40 ADB machine-side taper and a 22 mm connection that matches the respective toolholder's connection bore[22].

Figure 8: *Seco DIN40ADB-SM22-035-L1 C10 - TOOLING SA HOLDERS*

3.2. Tool Wear Metrology

To accurately quantify the tool wear progression and establish tool life criteria for the subsequent Colding modelling, a 2D measurement was applied. Tool wear was visually inspected and measured using an Olympus SZX7 stereo optical microscope[23]. During the machining trials, the cutting process was periodically interrupted to capture the wear. These data formed the basis for defining the tool life.

Figure 9: *Olympus SZX7*

3.3. Material Characterization

To understand the effect of tool wear on the workpiece surface integrity and to analyze the inherent microstructural differences between CGI 450 and SSF CGI 350, metallographic preparation and surface observations were conducted.

3.3.1. Grinding and Polishing

The fundamental challenge in the metallographic preparation of Compacted Graphite Iron (CGI) is to retain the vermicular graphite in its true three-dimensional shape and size, while preventing the softer matrix (especially the highly ductile ferrite in SSF CGI 350) from smearing and obscuring the graphite structure. To achieve a pristine mirror-like surface suitable for microscopic evaluation, a standardized mechanical grinding and polishing procedure was adopted, following the industry best practices recommended by Struers.[24]

The preparation sequence involved the following progressive steps:

- Plane Grinding: The machined workpiece samples were initially plane-ground using Silicon Carbide (SiC) foil with water cooling to ensure macroscopic flatness and remove primary cutting marks.
- Fine Grinding: To prevent graphite relief and retain edge sharpness, fine grinding was performed using a composite disc (MD-Largo) dosed with a 9 µm polycrystalline diamond suspension.
- Polishing: A rigorous, multi-step diamond polishing sequence was applied to systematically remove any residual deformation and smeared metal from the matrix. This involved consecutive polishing stages using diamond suspensions of 3 µm on an MD-Dac cloth, followed by 1 µm

on a softer MD-Nap cloth, and concluding with an ultra-fine sub-micron polish at 0.5 µm to achieve a defect-free mirror finish.

- Cleaning and Drying: To mitigate the high risk of rapid oxidation and corrosion, which is common in freshly polished cast irons, the samples were cleaned swiftly with cold water after the final polish, immediately rinsed with ethanol, and rapidly dried using a stream of warm air.

Figure 10: *Tegramin grinding and polishing machine*

3.3.2. Etching

To achieve a comprehensive microstructural analysis, a sequential dual-etching protocol was meticulously applied to the polished workpiece samples:

Primary Etching (Nital): The samples were initially etched using a standard 2% Nital solution (nitric acid in ethanol). As the fundamental etchant for cast irons, this step was essential to reveal the general matrix morphology and phase boundaries. Specifically, it allowed for the clear differentiation between the predominantly pearlitic structure of CGI 450 and the highly ductile matrix of SSF CGI 350. Under this etchant, the ferritic matrix in SSF CGI 350 appears distinctly white, while clearly delineating the internal grain boundaries of the ferrite.

Secondary Etching (Stead's Reagent): Because Nital alone cannot resolve phosphorus-rich microstructures, a secondary specialized etching process was performed using Stead's reagent which is a copper ammonium chloride solution. This reagent was applied specifically to highlight the steadite (phosphide eutectic). Stead's reagent works through selective deposition, leaving the steadite visible as a bright, distinct network primarily along the eutectic cell boundaries. Identifying these hard, brittle phosphide phases is crucial for machining analysis, as their presence can significantly influence local cutting forces and initiate micro-chipping on the cutting tools.

3.3.3. Alicona Microscopic Observation

Following the metallographic preparation and etching procedures, the microstructures of the workpiece samples were systematically examined. The observations were conducted utilizing the same Alicona microscope.

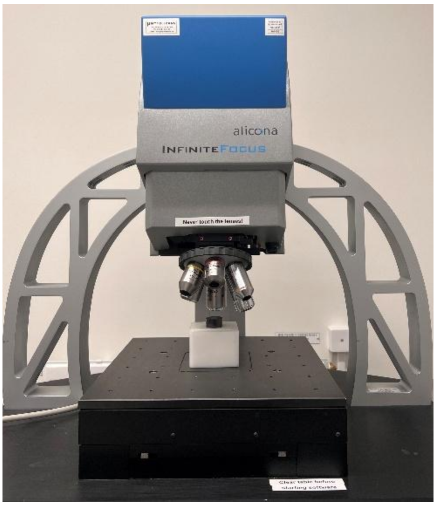

Figure 11: *Alicona*

To comprehensively capture the microstructural features at different scales, the optical evaluations were performed using both 5x and 50x objective lenses:

5x Objective: This magnification was employed to obtain a macro-level overview of the material matrix. It allowed for the broad assessment of the vermicular graphite distribution, the macroscopic phase proportions, and the overall uniformity of the eutectic cell boundaries revealed by Stead's reagent.

50x Objective: Critical for detailed, high-resolution microstructural characterization. At this magnification, the intricate features etched by the reagents were clearly resolved, specifically allowing for the close examination of the internal grain boundaries within the ferrite, the fine structure of the pearlite colonies in CGI 450, and the precise morphology of the phosphide eutectic (steadite) networks at the cell boundaries.

3.4. Micro-Morphological and Chemical Characterization

To investigate the microscopic wear mechanisms, advanced characterization was performed using a TESCAN scanning electron microscope (SEM) equipped with an Oxford Instruments Energy Dispersive X-ray Spectroscopy (EDS) system.

Figure 12: *Sem and EDS equipment*

3.4.1. Sample Preparation for SEM

Before the SEM evaluation, the inserts were cleaned in an ultrasonic ethanol bath for 10 minutes. This procedure was to remove loose graphite flakes and debris to preserving adhered material. Since the ceramic inserts are non-conductive, they were sputter-coated with a thin gold (Au) layer to prevent electron charging artifacts and ensure stable, high-resolution imaging.

3.4.2. SEM Imaging and Analytical Modes

The TESCAN SEM was operated in multiple detection modes to capture different aspects of the tool wear:

Secondary Electron (SE) Imaging: Used for high-resolution topographical characterization of the cutting edge to identify physical damage like micro-chipping and abrasive grooves.

Backscattered Electron (BSE) Imaging: Employed to provide atomic number contrast (Z-contrast), enabling clear visual differentiation between the heavy tool substrate and the lighter adhered workpiece material (Fe-based CGI).

3.4.3. EDS Chemical Analysis

Chemical analysis and elemental distribution mapping were performed through the AZtec software suite and Oxford Instruments integrated with the TESCAN system. The methodology focused on:

Elemental Mapping and Point Analysis: To visualize the spatial distribution of elements across the contact zones. Particular focus was placed on identifying Iron (Fe) and Silicon (Si) to quantify adhesion, as well as Magnesium (Mg).

Data Processing: Tracking the distribution of Mg is critical as it can deposit on the tool surface to form protective layers (TPL) under specific conditions[27].

3.5. Data Processing

Following the experimental wear measurements, the collected raw data was processed to establish the tool life models based on the Colding equation. The data processing workflow consisted of two steps: data extraction and computational modelling.

Initially, the macroscopic wear progression data obtained from the Olympus microscopy was recorded and analyzed using Microsoft Excel. For each specific cutting test, the wear curves were plotted. The exact tool life was determined by identifying the point where the flank wear reached VB = 300 μm. For tests where the measurement points did not land exactly on the 300 μm mark, linear interpolation was applied to calculate the precise equivalent cutting length and tool life duration.

Subsequently, to derive the Colding tool life models, the extracted data were processed using a Python script. This computational approach was utilized to translate the complex, multi-variable Colding mathematical framework into an executable algorithm. By employing numerical optimization and curve-fitting libraries within Python, the five fundamental constants of the Colding model K, H, M, N_0, and L were accurately computed for each successful tool-workpiece combination. This automated regression process ensured high accuracy in generating the final 3D tool life topographies and evaluating the machinability differences between CGI 450 and SSF CGI 350.

3.6. The Colding Model

The accurate prediction of tool life is a cornerstone of machining optimization. When selecting an appropriate tool life model, it is crucial to balance computational efficiency with predictive capability. While numerical methods such as the Finite Element Method (FEM) offer deep insights into initial cutting deformation, their extensive computational time renders them impractical for simulating macroscopic tool wear progression over several minutes or longer[25]. Consequently, empirical models remain the primary tool of industrial tool life prediction due to their computational efficiency and direct reliance on cutting data[25].

However, traditional empirical models such as Taylor equation, have limitations in multi-variable environments. The simplified Taylor equation primarily evaluates cutting speed, and its predictive curves inherently shift when other critical parameters are altered[25]. To address this limitation and capture the highly non-linear wear dynamics inherent to the high-speed milling of advanced cast irons, the advanced Colding tool life model is employed in this methodology.

As an extension of the Taylor equation, the Colding model incorporates Woxén's equivalent chip thickness[25]. This approach integrates multiple parameters such as feed rate, depth of cut, and tool geometry into a unified multi-dimensional tool life response surface.

In this study, the Colding model is used. While empirical models do not require a physical understanding of wear mechanisms to operate[25], this characteristic is used in this study. By establishing this mathematical baseline, any significant deviations observed between the theoretical Colding predictions and the experimental tool life data will serve as macroscopic indicators.

Determining the empirical constants of the Colding equation, presents a mathematical challenge. As highlighted in recent comparative studies on Colding [26], due to the highly non-linear nature of the tool life model and the complex 3D wear surface it represents, conventional linear regression methods frequently fail to converge or yield physically meaningless values. Therefore, a customized numerical optimization algorithm was developed to extract these constants.

The fundamental principle of the Colding tool life model is to establish a mathematical relationship between three primary machining variables: the cutting speed v_c, the equivalent chip thickness h_e, and the tool life T_{ratio}.

This tool life prediction model is characterized by 5 empirical constants, denoted as K, H, M, N_0, and L[5]. By accurately determining these constants, the model can provide a specific prediction of tool life T_{ratio} as a function of any chosen combination of cutting speed and chip thickness.

The generalized Colding relationship used in this study to calculate the cutting speed is expressed mathematically as follows:

$$v_c = e^{\left[K - \frac{(ln(h_e) - H)^2 - (N_0 - L \times ln(h_e)) \times ln\,(T_{ratio})}{4 \times M}\right]}$$ *Equation 1*

Where:

h_e: Equivalent chip thickness.

T_{ratio}: Tool time ratio.

v_c: Cutting speed (modeled).

K, H, M, N_0, L: Constants to be optimized.

The equivalent chip thickness h_e is calculated using the following formula:

$$h_e(f_z, a_p, r_\varepsilon, d_{DC}, a_e, Jay) = \frac{a_p \times fze(f_z, a_p, r_\varepsilon, d_{DC}, a_e, Jay)}{r_\varepsilon \times arccos\left(\frac{r_\varepsilon - a_p}{r_\varepsilon}\right) + \frac{fze(f_z, a_p, r_e, d_{DC}, a_e, Jay)}{2}}$$ *Equation 2*

Where:

f_z: Feed per tooth.

a_p: Depth of cut.

r_ε: Nose radius. In the case of round inserts, it is the same as tool radius.

d_{DC}: Tool diameter.

a_e: Radial engagement.

Jay: Scaling constant.

$fze(f_z, a_p, r_\varepsilon, d_{DC}, a_e, Jay)$: Equivalent feed per tooth.

The tool time ratio T_{ratio} is calculated using the following formula:

$$T_{ratio}\left(l_w, f_{speed_{CC}}, passes_{CC}, f_z, a_p, r_e, d_{DC}, a_e, Jay\right) = t_{total}\left(l_w, f_{speed_{CC}}, passes_{CC}\right) \times \frac{l_{arc_{he}}(f_z, a_p, r_\varepsilon, d_{DC}, a_e, Jay)}{\pi \times D_w(f_z, a_p, r_\varepsilon, d_{DC})} \qquad \textit{Equation 3}$$

Where:

l_w: Length of pass.

$f_{speed_{CC}}$: Feed speed.

$passes_{CC}$: Number of passes.

f_z: Feed per tooth.

a_p: Depth of cut.

r_ε: Nose radius. In the case of round inserts, it is the same as tool radius.

d_{DC}: Tool diameter.

a_e: Radial engagement.

Jay: Scaling constant.

$l_{arc_{he}}(f_z, a_p, r_\varepsilon, d_{DC}, a_e, Jay)$: Arc length.

$D_w(f_z, a_p, r_\varepsilon, d_{DC})$: Working diameter.

To calculate these constants, a numerical optimization algorithm was developed in Python. The evaluation process consists of 2 primary steps:

First is logarithmic transform the objective function. To stabilize the optimization process, the evaluation is performed entirely within the logarithmic domain. By taking the natural logarithm of both sides of the original Colding equation, the relationship is transformed into a smoother polynomial form:

$$ln(v_c) = K - \frac{(ln(h_e) - H)^2}{4 \times M} - (N_0 - L \times ln(h_e)) \times ln\,(T_{ratio}) \qquad \textit{Equation 4}$$

Operating in the logarithmic space prevents the optimization algorithm from being disproportionately skewed by the extreme numerical values of high cutting speeds. The objective function for the optimization algorithm was thus defined to minimize the residual sum of squares (RSS) between the experimental logarithmic cutting speeds $ln(v_{c,exp})$and the modeled values $ln(v_{c,mod})$.

Second is use hybrid optimization via grid search and Powell's method. Since the five constants are highly coupled, the error surface contains multiple local minima. Traditional gradient-based algorithms are prone to getting trapped in these local minima, leading to inaccurate parameter estimation. To overcome this, a hybrid optimization strategy was implemented using the SciPy library:

- Grid search initialization: A multi-start grid search algorithm was programmed to systematically generate a wide array of initial guesses across predefined parameter boundaries. This ensures that the algorithm explores the entire parameter space.
- Powell's optimization method: Each set of initial guesses was subsequently fed into Powell's conjugate direction method. As a robust, derivative-free optimization algorithm, Powell's method is highly effective in navigating the non-linear Colding error surface to pinpoint the true global optimum.

Through this advanced computational approach, the constants (K, H, M, N_0, L) were successfully extracted for each tool-material combination, ensuring that the resulting models mathematically reflect the true physical wear mechanisms observed during the milling trials.

To quantitatively evaluate the accuracy and reliability of the optimized Colding parameters for each tool-workpiece combination, the Mean Absolute Percentage Error (MAPE), denoted in this study as the error (ERR), was employed as the primary statistical metric. The MAPE calculates the average relative deviation between the experimentally measured cutting speeds ($v_{c,\,exp}$) and the theoretical cutting speeds predicted by the model ($v_{c,\,mod}$), expressed as a percentage:

$$ERR = \frac{100\%}{n} \sum_{j=1}^{n} \left| \frac{v_{c,exp} - v_{c,mod}}{v_{c,exp}} \right| \times 100\% \qquad \textit{Equation 5}$$

Where:

n: The total number of experimental points.

j : Each individual experimental trial.

By utilizing MAPE, the evaluation provides a standardized, scale-independent measure of the model's predictive performance across diverse machining conditions.

4. Results

4.1. Workpiece

To understand the tool wear mechanisms, the microstructures of the workpiece materials CGI 450 and SSF 350 were examined using optical metallography.

The samples were analyzed in unetched conditions to evaluate graphite morphology, and subsequently etched with Nital and Stead's reagent to reveal the matrix phases and elements.

The results of these Alicona analyses are compiled into 2 summary figures below. The micrographs are arranged by the top, middle, and bottom rows present the unetched, Nital etched, and Stead's reagent etched conditions, respectively. For each condition, the left column provides a macroscopic overview at 5x magnification, while the right column details the microstructural features at 50x magnification.

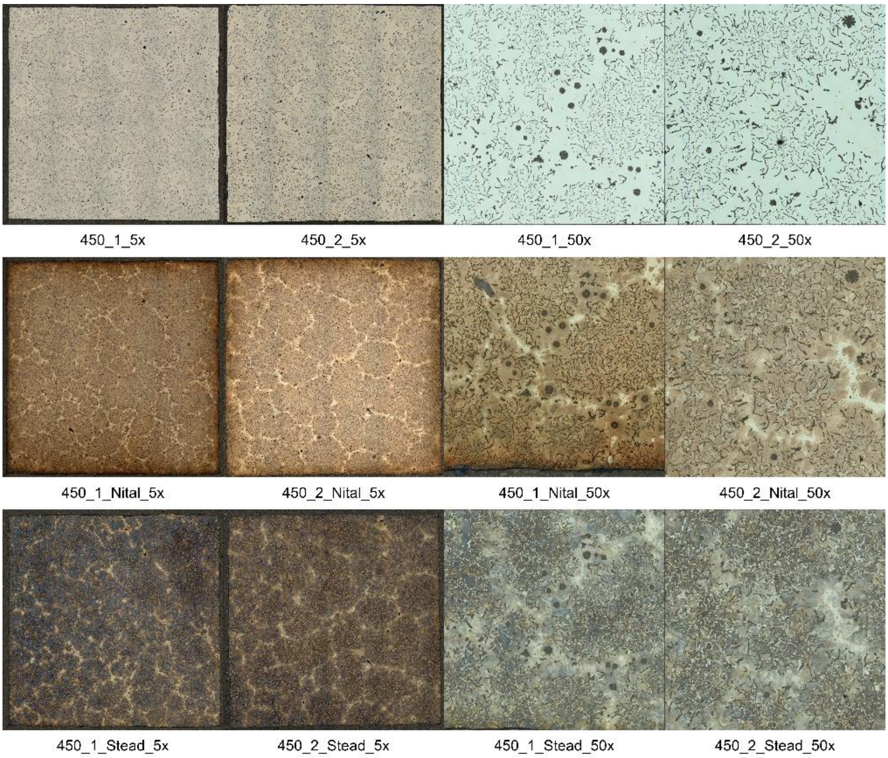

Figure 13: *CGI450 Alicona results*

Figure 13 presents the metallographic summary of the CGI 450 workpiece. As shown in the unetched condition, the microstructure reveals a mainly compacted graphite morphology, characterized by its interconnected, worm-like shape, alongside a minor fraction of isolated graphite nodules. This specific graphite geometry is the defining characteristic of CGI.

Upon etching with Nital, the matrix is revealed to be pearlitic, interspersed with distinct ferrite halos surrounding the graphite particles.

Last, the results of Stead’s reagent etching show the eutectic cell boundaries. Solute elements rejected during the final stages of solidification are marked by the dark copper deposition. This confirms the highly heterogeneous structure of the high-strength CGI matrix.

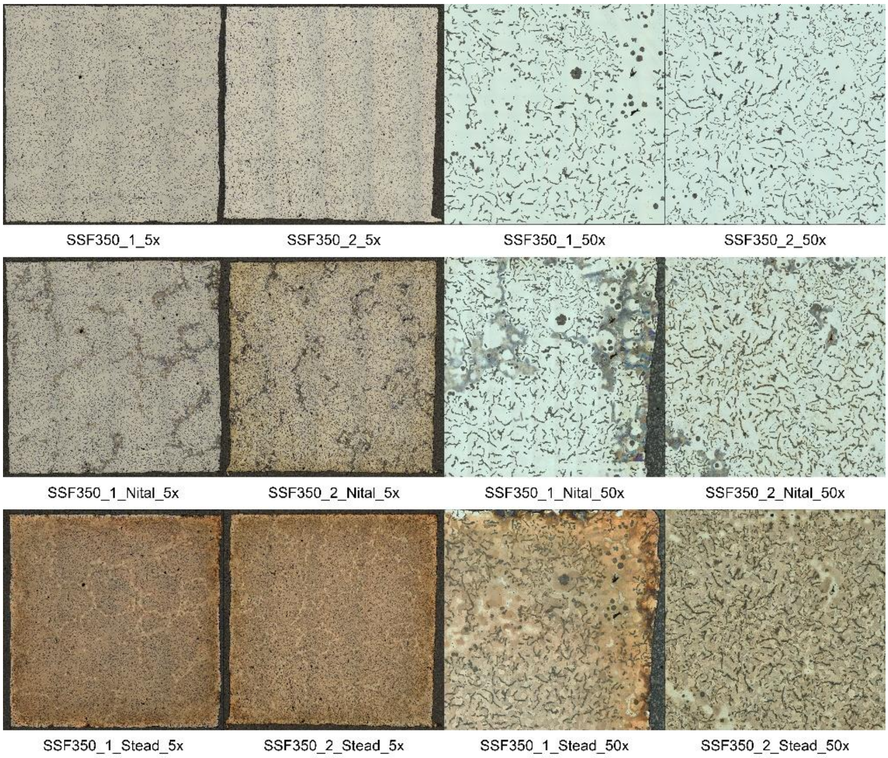

Figure 14: *SSF350 Alicona results*

Figure 14 illustrates the microstructural verification of the SSF 350 workpiece. The unetched micrographs confirm a nodular graphite morphology, ensuring the high ductility inherent to spheroidal graphite iron.

The Nital etch confirms the overall matrix architecture, displaying a fully ferritic matrix devoid of pearlite. This confirms that the SSF 350 workpiece possesses a highly ductile, fully ferritic matrix strengthened by severe Silicon microsegregation. SSF 350 relies on a high Si content for solid solution strengthening. This high Si characteristic is captured by the Stead's reagent etch. Si repels the copper deposition from the reagent, leaving the Si-rich ferritic matrix light in appearance.

4.2. Tool wear

4.2.1. Qualitative Wear

The qualitative evaluations of the worn cutting edges were performed using the TESCAN SEM. The results focus on identifying the wear modes, such as abrasive wear, adhesive wear, and physical degradation like micro-chipping.

For ceramic, Figure 15 illustrates the wear morphology of the ceramic insert after machining the CGI 450. The BSE image on the right side shows relatively uniform grey-scale contrast, indicating minimal workpiece material adhesion due to the high chemical inertness of the ceramic substrate. The SE image on the left reveals severe localized mechanical degradation, including flaking and spalling near the cutting edge. These observations indicate that the dominant failure mechanism for the ceramic tool was mechanically induced brittle fracture under severe thermo-mechanical loading.

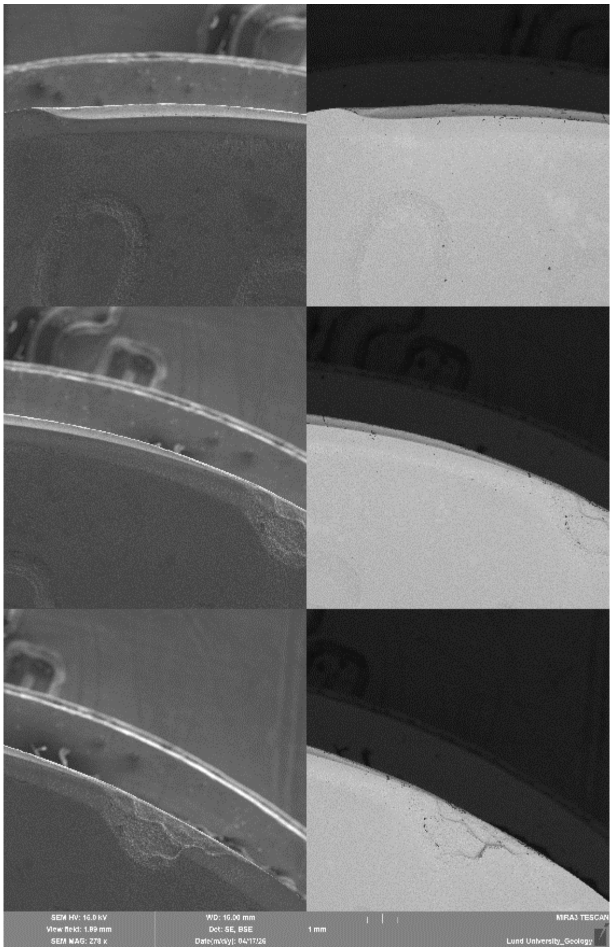

Figure 15: *Ceramic _CGI450_fz015vc650*

And for CC, Figure 16, Figure 17 and Figure 18 present the wear characteristics of the CC insert after machining the SSF 350. Figure 16 reveals progressive flank wear. The wear progression appears relatively stable compared with the other tool materials. In Figure 17, distinct compositional contrast is visible across the worn region, confirming substantial material transfer and the formation of a stable Built-Up Layer (BUL). Figure 18 shown the thermal crack in the results. These observations indicate dominant adhesive wear behaviour together with localized thermo-mechanical fatigue effects.

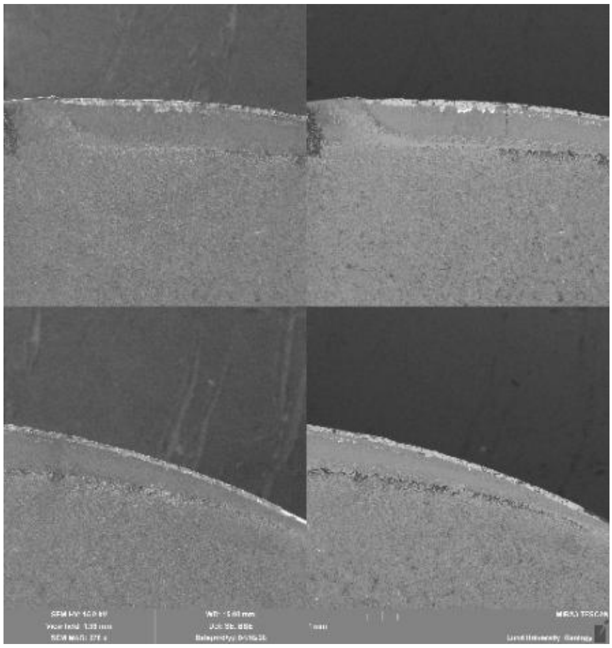

Figure 16: *CC _SSF350_fz277vc480*

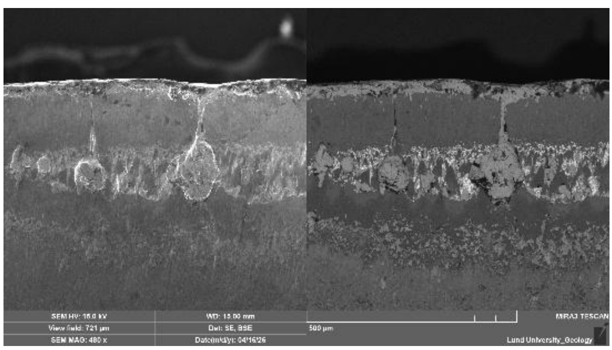

Figure 17: *CC _SSF350_fz554vc480*

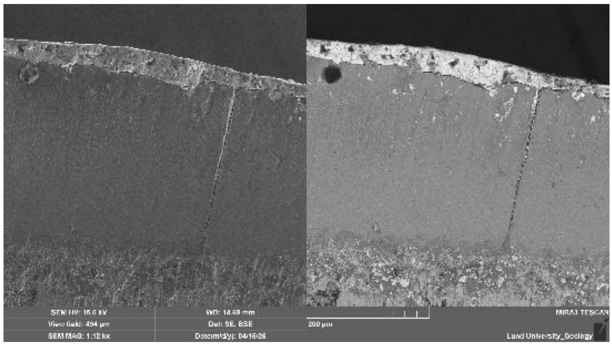

Figure 18: *CC _SSF350_fz477vc295*

Finally, Figure 19 displays the wear progression of the cBN insert during machining of CGI 450. The SE image reveals combined crater wear and abrasive flank wear under severe machining conditions. Localized edge chipping is also observed near the cutting edge. These wear features indicate intense thermo-mechanical interaction at the tool-chip interface under high cutting speeds. In addition, the BSE image shows clear compositional contrast, suggesting that adhesive material transfer also contributed to the overall wear progression.

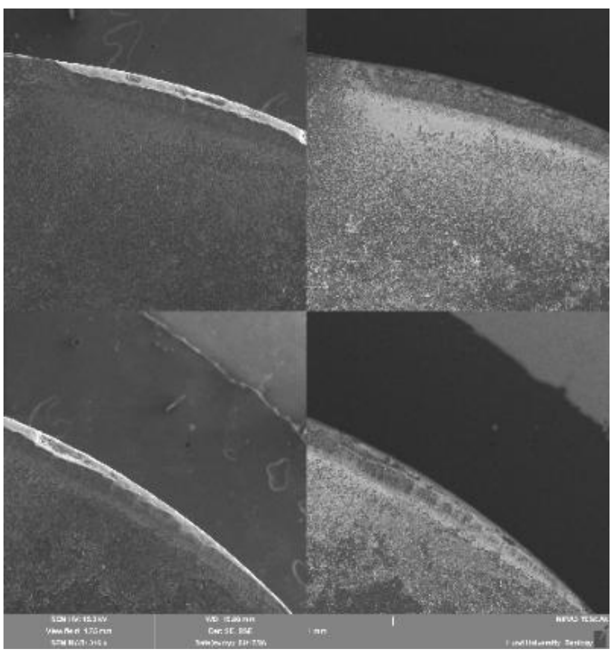

Figure 19: *cBN _CGI450_fz005vc1000*

4.2.2. Experimental tool life data

The experimental results provide a comprehensive evaluation of tool performance across different workpiece materials, highlighting significant variations in durability and machining efficiency based on tool-material combinations and cutting conditions.

In general, optimal performance is achieved by balancing cutting speed and feed rate to minimize flank wear while maintaining a stable material removal rate. For high-strength cast irons, tool selection is the primary factor in determining whether the process prioritizes maximum volume removal or rapid processing speeds, with specific parameters like low feed rates often proving essential for extending tool life during high-speed operations.

For CGI450, cBN tools emerge as the superior choice for both endurance and speed, as evidenced in Figure 24 and Figure 25, where they achieve a maximum volume removal exceeding 2500000 mm^3 and peak MRR near 40000 mm^3/min. Optimal conditions for cBN involve low feed rates (0.05 mm/rev) and high speeds (1000–1500 m/min). In contrast, Ceramic tools show moderate efficiency but are highly sensitive to speed. Figure 20 shows that at 1200 m^3/min, wear accelerates rapidly, limiting total volume to approximately 1200000 mm^3. Cemented carbide tools are the slowest for this material, with Figure 23 showing rates below 35 mm^3/min, making them best suited for low speed, high precision tasks where stable, linear wear is required.

For SSF CGI 350, cemented carbide provides the highest durability, with Figure 28 indicating a total removal capacity surpassing 4,500,000 mm^3 under low-speed conditions. While cemented carbide offers the greatest volume, ceramic tools provide the highest processing efficiency for this material. Figure 27 demonstrates that ceramic tools consistently maintain MRR levels above 45 mm^3/min. However, Figure 26 reveals a significant trade off, as high feed rates cause rapid tool wear that restricts the total processed volume to under 1000000 mm^3. Thus, cemented carbide is ideal for long duration stability, while ceramic is preferred for short duration, high efficiency machining of SSF CGI 350.

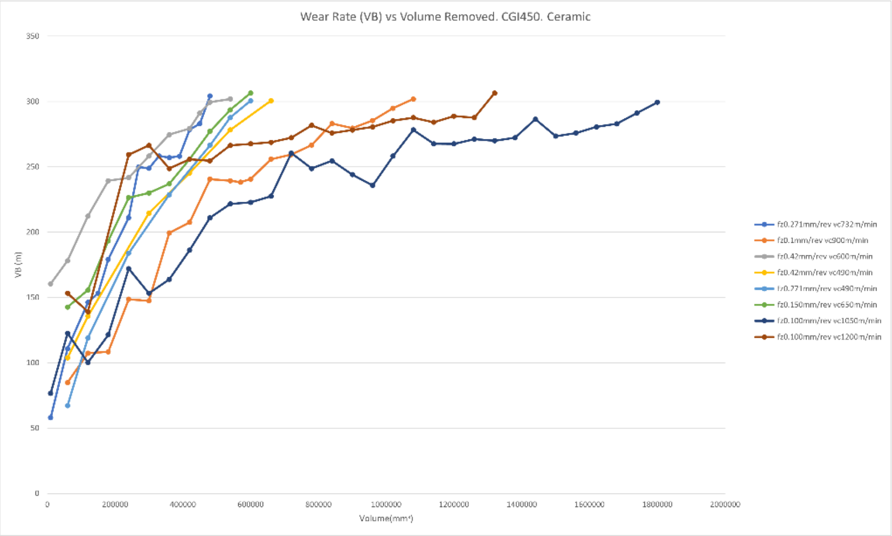

Figure 20: *Wear Rate (VB) vs Volume Removed. CGI450. Ceramic*

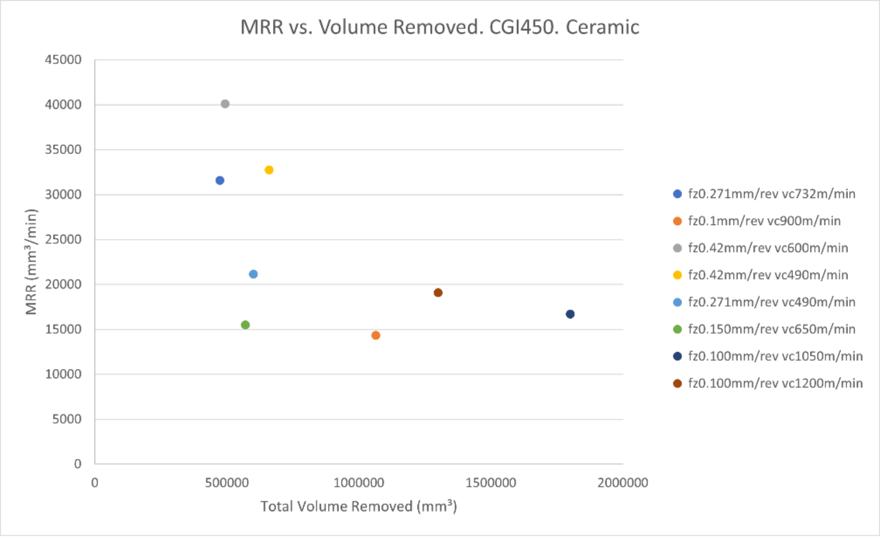

Figure 21: *MRR vs. Volume Removed. CGI450. Ceramic*

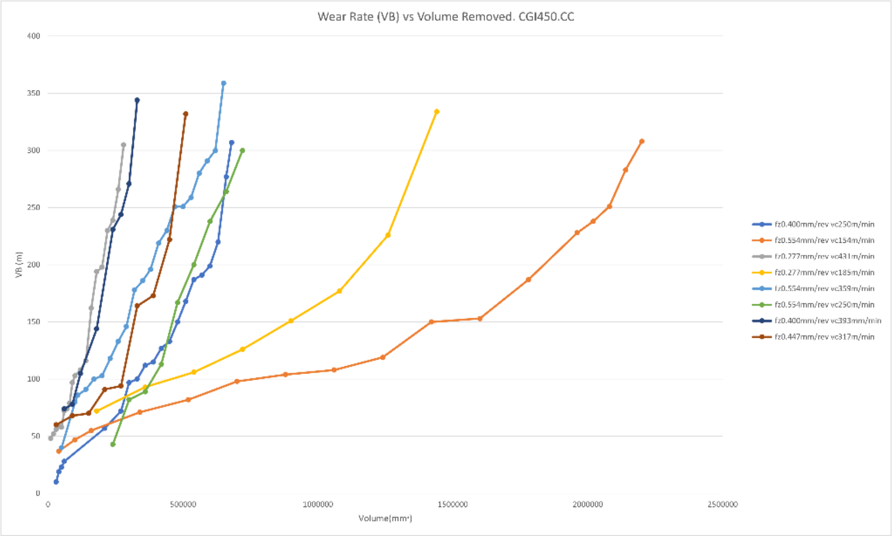

Figure 22: *Wear Rate (VB) vs Volume Removed. CGI450.CC*

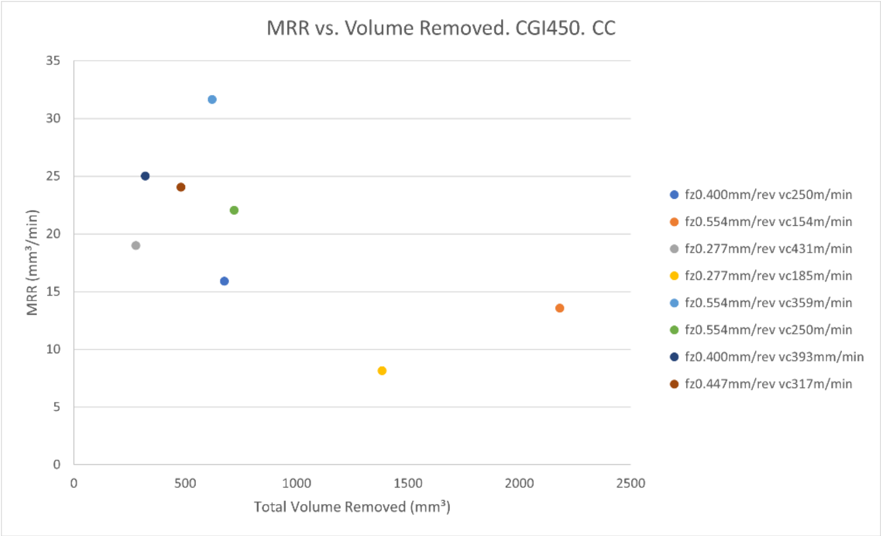

Figure 23: *MRR vs. Volume Removed. CGI450. CC*

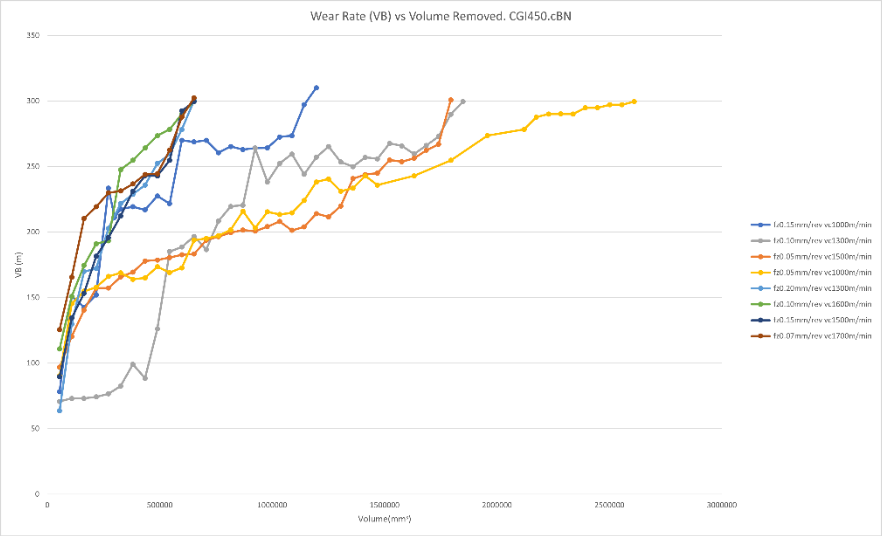

Figure 24: *Wear Rate (VB) vs Volume Removed. CGI450.cBN*

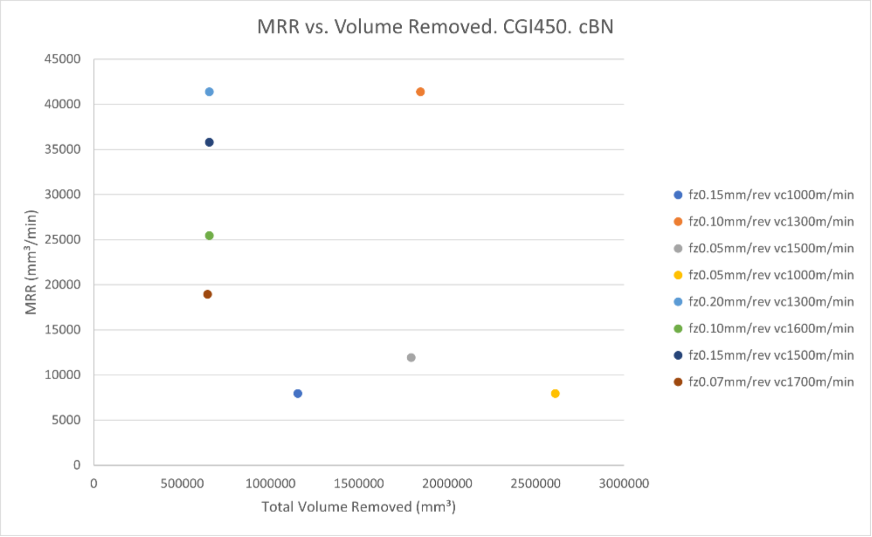

Figure 25: *MRR vs. Volume Removed. CGI450. cBN*

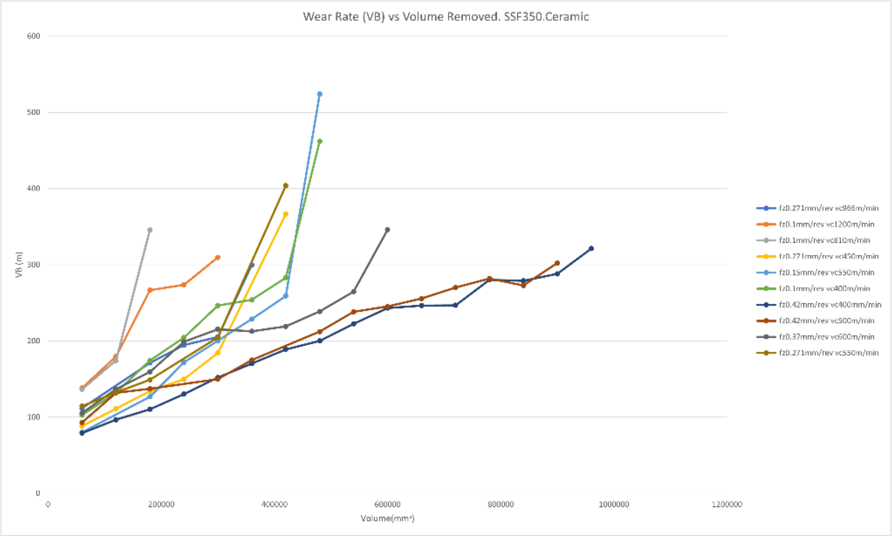

Figure 26: *Wear Rate (VB) vs Volume Removed. SSF350.Ceramic*

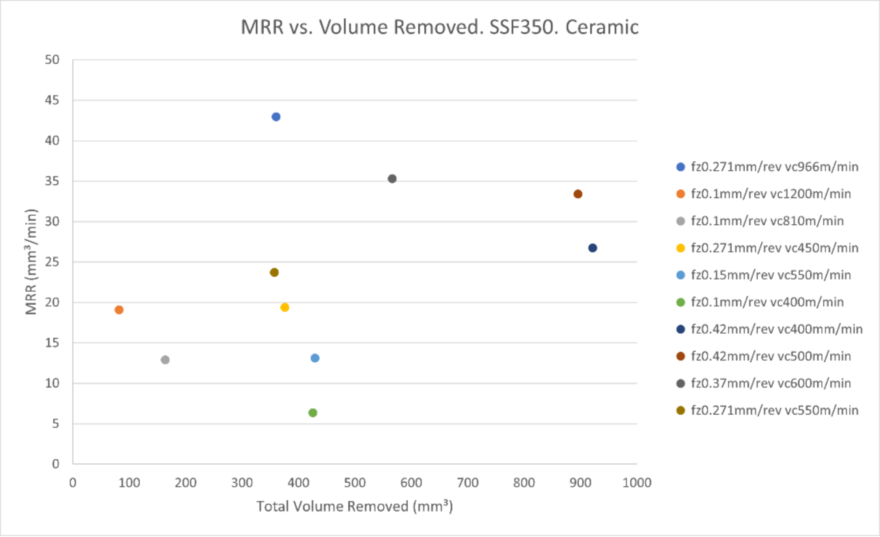

Figure 27: *MRR vs. Volume Removed. SSF350. Ceramic*

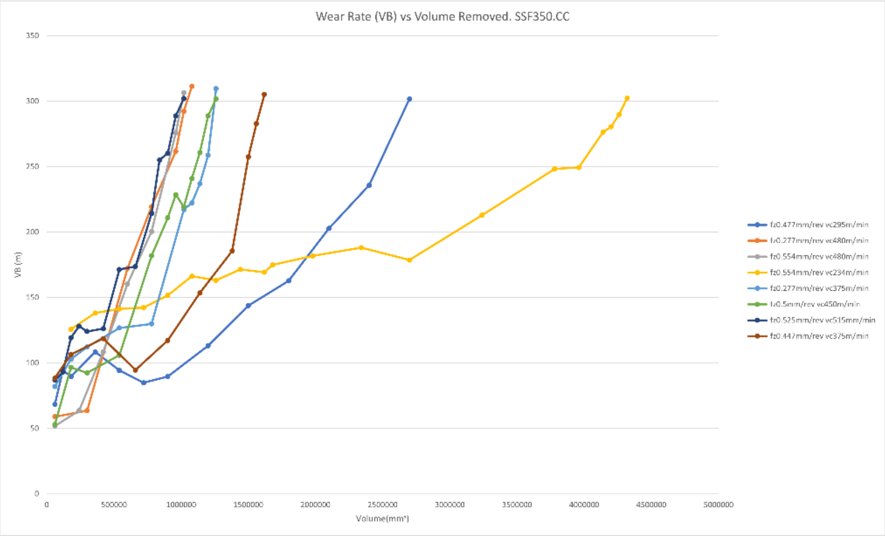

Figure 28: *Wear Rate (VB) vs Volume Removed. SSF350.CC*

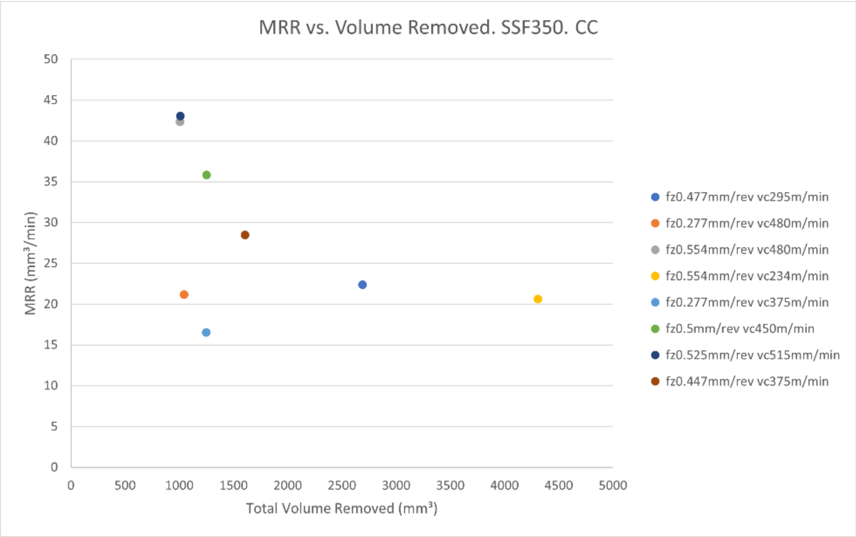

Figure 29: *MRR vs. Volume Removed. SSF350. CC*

4.2.3. The excluded case: cBN tool behaviour on SSF CGI 350

In the machining of SSF CGI 350, cBN tools exhibited a performance failure. Among all of the 8 tests, the first test resulted in a catastrophic tool fracture during the initial cutting pass, rendering the data unsuitable for further analysis. Consequently, this specific run is excluded from result figures. The remaining 7 tests, while not suffering from immediate fracture, showed high wear rates. These confirm that the combination of cBN tools and SSF CGI 350 is unfavorable under the tested conditions.

Experimental data in Figure 30 reveals a performance gap when utilizing cBN tools on SSF CGI 350 compared to CGI 450 reference. In the machining of CGI 450, cBN tools exhibited high productivity, achieving a total volume removed of over 2,500,000 mm^3 with material removal rates reaching approximately 40,000 mm^3/min. In contrast, the tests on SSF CGI 350 showed that cBN tools failed almost immediately. In Figure 31, the MRR for this combination was significantly lower, fluctuating only between 0 and 70 mm^3/min, and the total volume of material removed before tool failure was restricted to less than 350 mm^3. Furthermore, the wear rate for SSF CGI 350 climbed sharply to between 300 and 500 μm within an extremely small volume of removed material, indicating rapid and catastrophic deterioration of the cutting edge.

The catastrophic failure of the cBN tool during the initial pass on SSF CGI 350 can be attributed to a severe thermo-mechanical mismatch between the tool's inherent brittleness and the workpiece's highly ductile microstructure. As Zhu et al.[27] noted, elevated temperatures during CGI machining severely exacerbate adhesive wear, leading to the pull-out of cBN grains. Furthermore, the softer SSF CGI 350 promotes continuous chip formation. Shown in Section 3.3, the SSF CGI 350 matrix is basically ferritic and lacks abrasive phosphides. Consequently, the rapid failure was not driven by hard-particle impact or abrasion, but rather by severe adhesion. Due to the highly ductile and sticky nature of this ferritic matrix, massive adhesion and welding to the cBN rake face likely occurred instantly upon engagement under high cutting pressures.

Furthermore, even when catastrophic fracture was avoided, this continuous and aggressive adhesion-driven degradation explains the overall poor performance and rapid wear rates of cBN tools throughout the entire SSF CGI 350 experimental series.

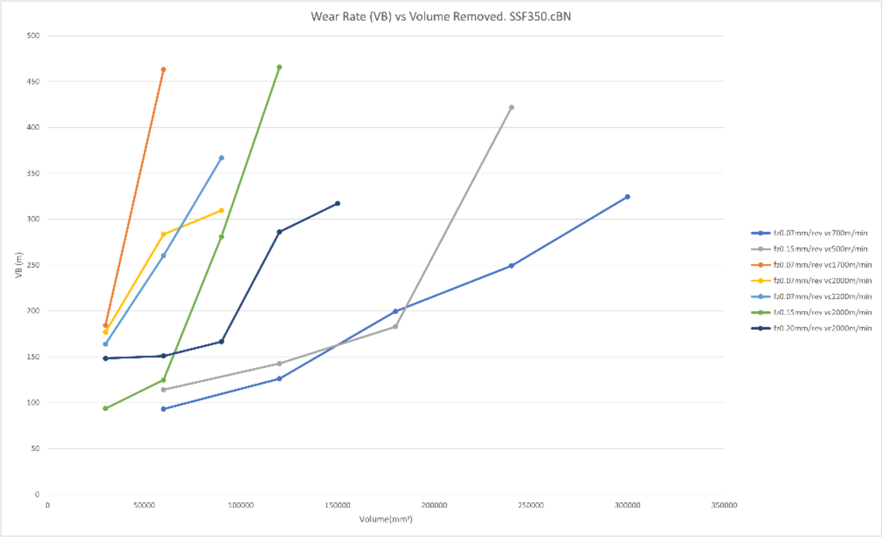

Figure 30: *Wear Rate (VB) vs Volume Removed. SSF350.cBN*

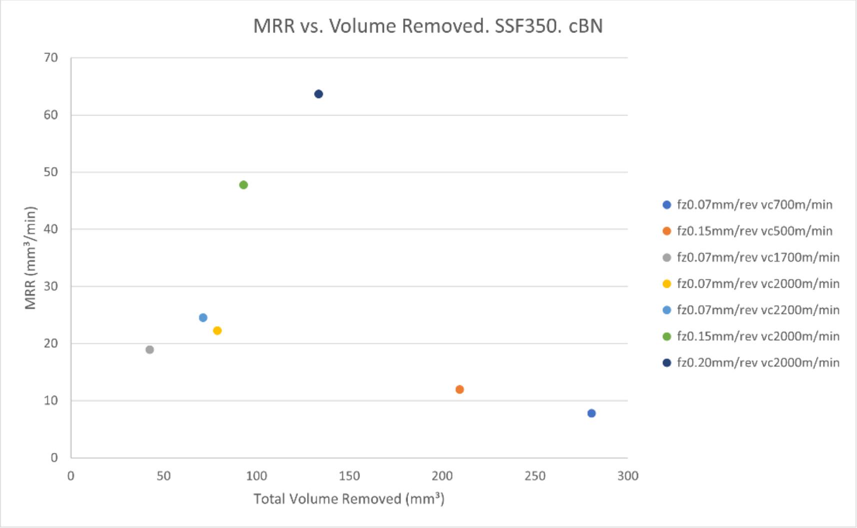

Figure 31: *MRR vs. Volume Removed. SSF350. cBN*

4.2.4. Chemical Analysis

To identify the elemental composition of the adhered layers and find out the wear mechanisms, Energy Dispersive X-ray Spectroscopy (EDS) was performed on the worn edges. Based on the compositional contrast observed in the BSE micrographs, specific areas were selected for elemental mapping.

4.2.4.1. Ceramic

For the ceramic inserts, the one that machined the CGI 450 was test in EDS. While the chemical wear mechanisms remained consistent across all tests, the results of the optimal cutting conditions v_c = 1050 m/min and f_z = 0.10 mm are presented here as the most representative example.

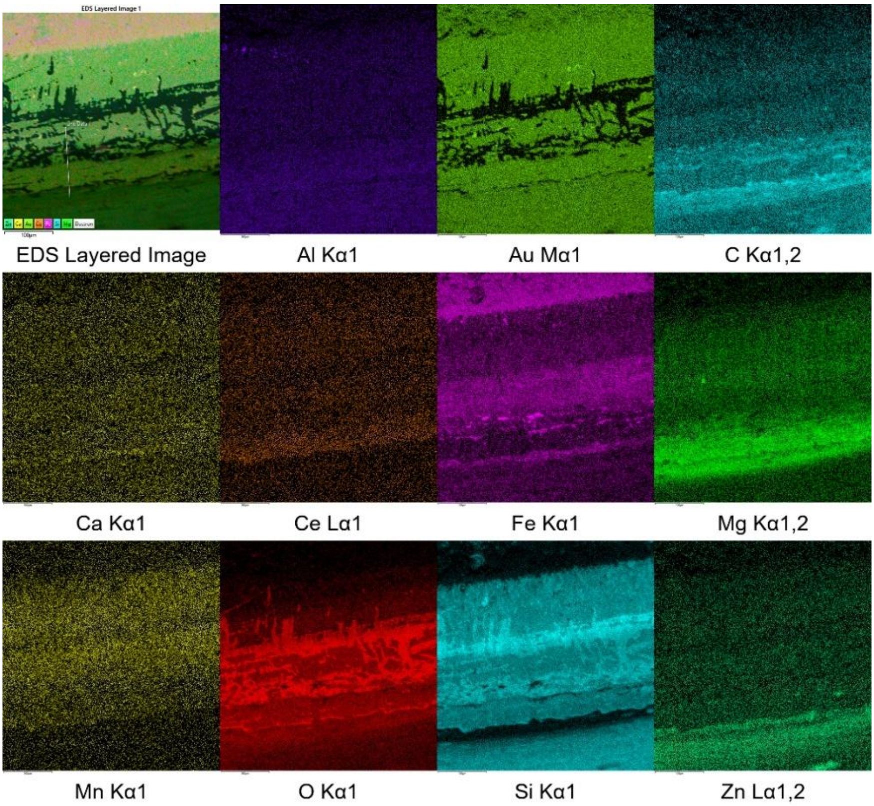

Figure 32: *EDS results of the ceramic insert*

Figure 32 shows the elemental distribution for this ceramic insert. First, the figure characterizes the base ceramic substrate, which is mainly composed of Silicone (Si), Aluminum (Al), and Magnesium (Mg). Also, trace amounts of rare-earth elements such as Cerium (Ce) and Ytterbium (Yb) were detected. This may be because they are typically employed as advanced sintering additives to enhance high-temperature fracture toughness[29].

Beyond the substrate composition, the EDS results also showed a similar position of Iron (Fe) and Oxygen (O) along the wear zone. This indicates the presence of adhered workpiece material on the insert and proves the formation of an iron oxide layer. The presence of Fe and O represents material transfer from the workpiece driven by the high mechanical and thermal loads.

Additionally, the EDS results reveal another critical distribution of Mg. Rather than being uniformly dispersed, the Mg signal displays distinct localized concentrations. These concentrations overlap with both Si and O within the adhered layer. This specific elemental co-localization points to the formation of Mg-Si-O deposits[30]. Mg comes from the workpiece material, and Si is in the ferritic matrix and ceramic. Under the thermal and mechanical loads of high-speed machining, these elements react with environmental oxygen. This high-temperature solid-state reaction forms a robust Mg-Si-O protective deposit. While precise crystallographic identification requires techniques beyond EDS, recent studies on CGI machining[30] suggest that these Mg-Si-O deposits likely crystallize as orthopyroxene structures, such as $(Mg,Fe)Si_2O_3$, or potentially as forsterite Mg_2SiO_4. This layer functions as a high-temperature solid lubricant and thermal barrier. It reduces friction and shields the underlying tool substrate from direct mechanical attrition. Consequently, this Mg-Si-O layer suppresses wear and prolongs tool life.

To further quantify the spatial distribution and elemental gradient across this specific tool-chip interface, an EDS line scan analysis was performed. As illustrated in Figure 33, the scan line traverses directly from the ceramic substrate through the dark adhered layer.

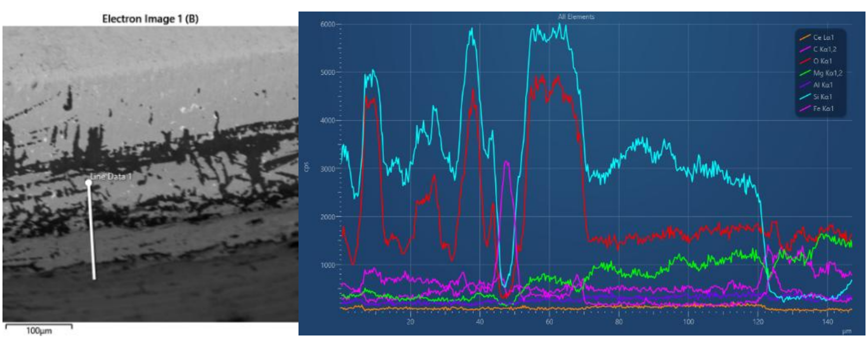

Figure 33: *EDS line scan result of the ceramic insert*

Moving along the scan path, a distinct boundary is observed at approximately the 120 μm mark. Here, the signal intensity of the primary element Si experiences a drop, which is match the grow in Fe and Mg concentration.

4.2.4.2. CC

For the CC inserts, EDS were evaluated across 6 parameter sets on machining SFF 350. The optimal parameter set v_c = 234 m/min and f_z = 0.554 mm is presented here as a representative case.

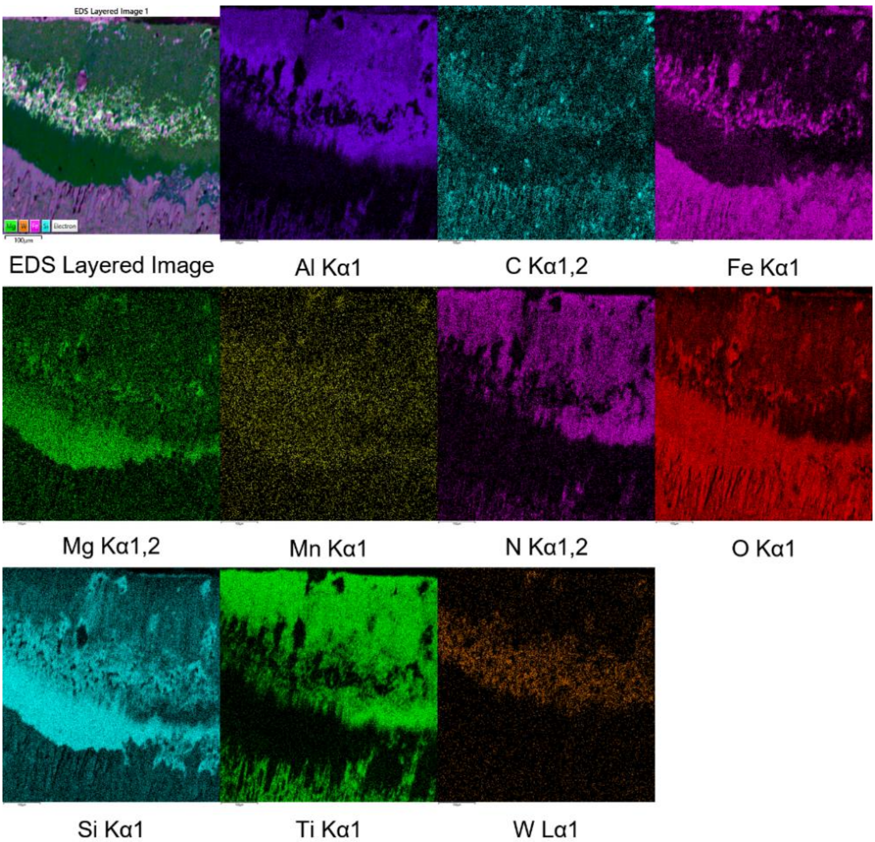

Figure 34: *EDS results of the CC insert*

In Figure 34, the maps show the Tungsten (W) rich substrate and the multi-component PVD coating, clearly identifiable by Titanium (Ti), Al, Si, and Nitrogen (N). The most critical revelation from the EDS analysis is the decisive role of Mg transferred from the SSF 350 workpiece. In this optimal parameter set, the elemental maps display a profound, localized concentration of Mg heavily overlapping with Si and O.

Across all 6 tests, results show that while the Mg-Si-O layer always tends to form, the tool life is dictated by the layer's integrity. In the poorly performing parameter sets, the Mg signal is usually sparse. The better thermomechanical conditions in the optimal cutting parameters help to preserve this layer longer. Comparing between different parameters, the Mg-Si-O layer stays longer under high cutting speed and feed rate.

4.2.4.3. cBN

For the cBN insert, EDS mapping and line scan analyses were conducted on the worn cBN insert after machining CGI 450 at v_c = 1000 m/min and f_z = 0.05 mm. The results reveal a similarity to the ceramic tools.

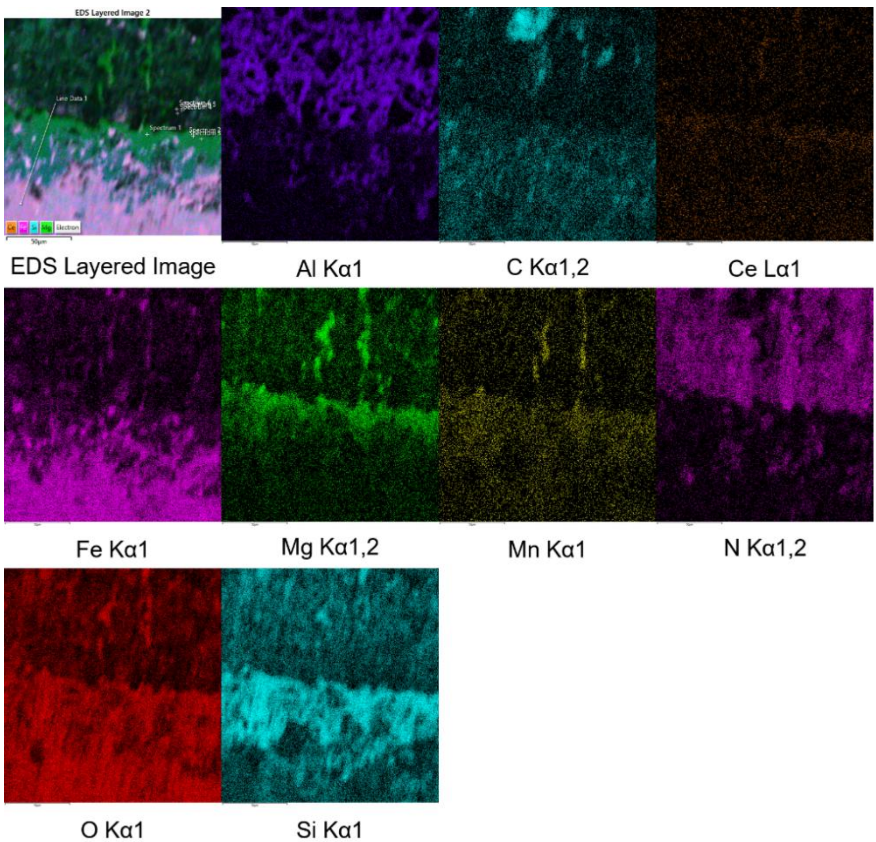

Figure 35: *EDS results of the cBN insert*

Figure 35 illustrates the comprehensive elemental distribution. First, the maps characterize the super-hard PcBN substrate and its ceramic binder phase. This is identified by the presence of N, Si, and Al. At the cutting edge, the maps display a large amount of Fe and O. Similar to previous observations, this confirms material transfer. Moreover, same to other inserts, Mg is also found in the cBN insert. As shown in the line scan Figure 36, there is a distinct and continuous band of Mg localized at the interface. And this Mg signal overlaps with Si and O.

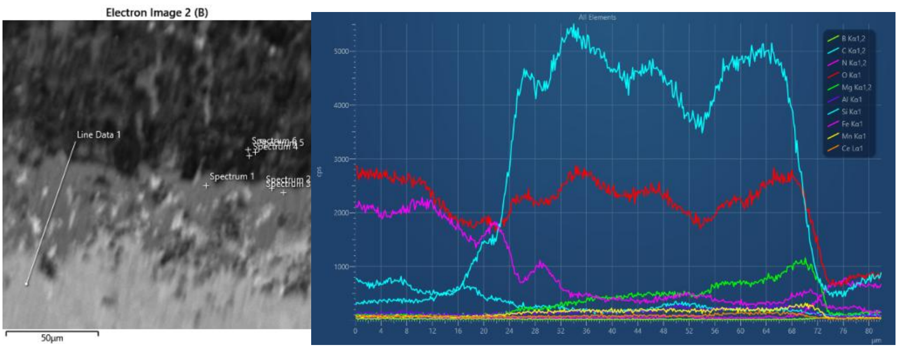

Figure 36: *EDS line scan result of the cBN insert*

These provides validation for the previously proposed theory that the Mg-Si-O layer formed during machining can protect inserts' coating. This protective layer separates the cBN substrate from the abrasive iron flow, providing high-temperature solid lubrication and thermal shielding.

Consequently, the EDS analysis confirms that the dynamic formation of this Mg-Si-O composite barrier is not isolated to specific tool materials, but is a fundamental, universal interfacial mechanism governing tool wear and longevity when machining CGI at elevated speeds.

4.3. Tool life modelling

Following the strategy detailed in the methodology, the 5 Colding constants (K, H, M, N_0, and L) were successfully extracted for each tool-workpiece combination. The optimized parameters, alongside their corresponding prediction errors (ERR), are systematically summarized in Table 1.

The wear data for the cBN tool machining SSF CGI 350 was excluded from the Colding modelling process. The machining tests revealed catastrophic tool failure at a very early stage. Post-machining inspections showed severe adhesive and chemical wear. The cBN material proved unsuitable for this highly ferritic workpiece. Thus, the tool did not exhibit a normal or stable steady-state wear phase. The model requires a predictable and continuous wear progression to calculate reliable constants. Applying the mathematical model to this highly unstable degradation would yield invalid results. The raw empirical data alone sufficiently proved the complete incompatibility of this tool-workpiece pair. Therefore, further mathematical optimization for this specific case was unnecessary.

Table 1: *Summary of the optimized Colding parameters and prediction errors*

Workpiece material	**Tool material**	**K**	**H**	**M**	**N_0**	**L**	**Prediction Error (%)**
CGI 450	Ceramic	17.74047524	34.08132249	32.47229197	2.19361149	-0.57858713	7.7577
	Cemented Carbide	7.14727586	-6.93856640	6.60785292	0.30862424	0.01350959	4.1743
	cBN	9.96412515	-12.58580473	8.80585423	0.19533138	0.01483319	6.2352
SSF CGI 350	Ceramic	7.19346406	-4.04832824	23.23138343	0.72179953	-0.07950401	8.7678
	Cemented Carbide	8.31967407	-4.31607861	0.66115652	-0.46099152	0.34148588	1.0716

An initial statistical evaluation reveals the exceptional robustness of the customized Python optimization algorithm. Across all tested combinations, the mean absolute percentage errors remained below 9%. Specifically, the CC and cBN inserts exhibited outstanding mathematical convergence. The models for CC machining SSF 350, CC machining CGI 450, and cBN machining CGI 450 yielded extremely low prediction errors of 1.0716%, 4.1743%, and 6.2352%, respectively. Furthermore, the Ceramic inserts also demonstrated strong mathematical fits, with errors of 7.7577% and 8.7678% when machining CGI 450 and SSF 350, respectively.

From a purely statistical perspective, the optimization successfully minimized the residuals across all matrices. In the summary table, the Colding model optimization algorithm demonstrated stableness in fitting the cutting parameters across different machining scenarios.

However, the results plots reveals singularities that contrast with the high statistical accuracy. In a standard Colding plot, an increase in equivalent chip thickness should generally correspond to a monotonic decrease in the permissible cutting speed to maintain a constant tool life[25].

While the models for ceramic cutting SSF350, CC cutting CGI 450, and cBN cutting CGI 450 follow this expected trend(Figure 39, Figure 41 and Figure 45), singularities are observed in the remaining plots.

In Figure 37 and Figure 43, there are singularities in the plots for ceramic machining CGI 450 and CC machining SSF 350. In these 2 specific machining cases, despite having low mathematical errors, the iso-life curves exhibit distinct unphysical behaviours. Within specific ranges of h_e, the tool-life curves unexpectedly intersect with one another or invert their slopes, indicating that a higher cutting speed would paradoxically result in the same tool life[25].

The coexistence of highly accurate statistical fits and severe geometric singularities indicates a fundamental conflict: while the numerical algorithm successfully minimized the mathematical residuals, the resulting polynomial surfaces in Figure 38 and Figure 44 do not represent standard steady-state mechanical wear.

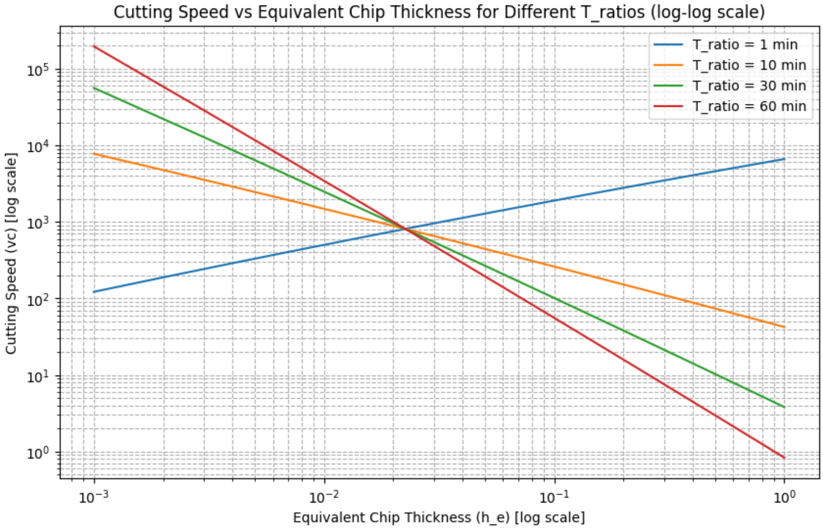

Figure 37: *CGI 450 Ceramic Cutting Speed vs Equivalent Chip Thickness for Different T_ratios.*

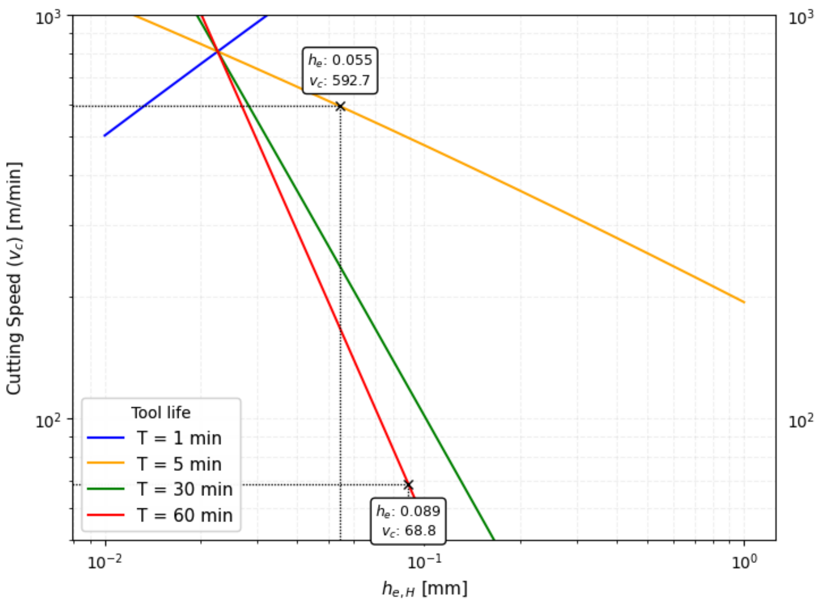

Figure 38: *CGI 450 Ceramic Colding results h_e.*

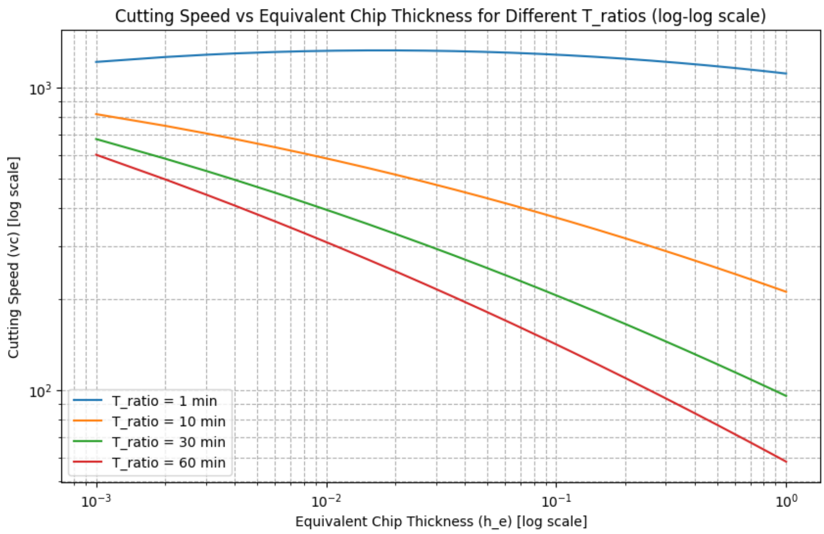

Figure 39: *SSF350 Ceramic Cutting Speed vs Equivalent Chip Thickness for Different T_ratios.*

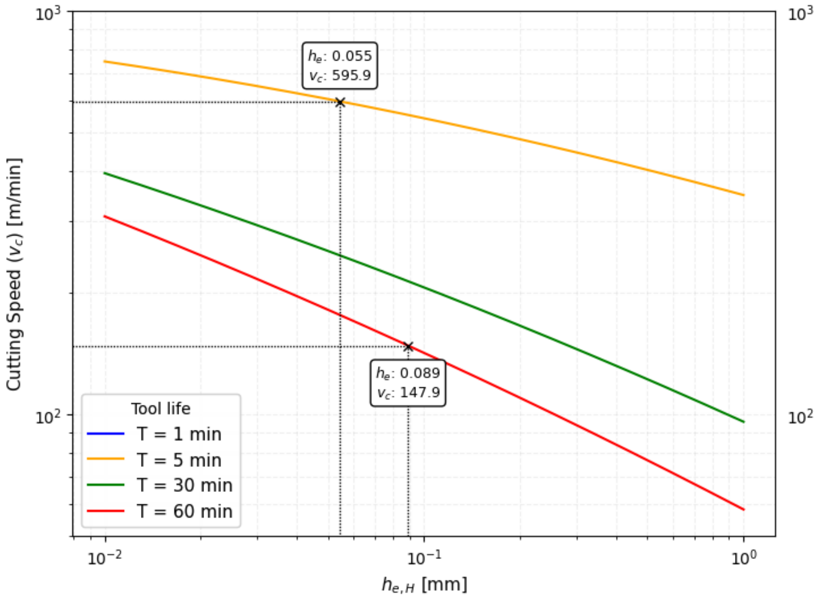

Figure 40: *SSF350 Ceramic Colding results h_e.*

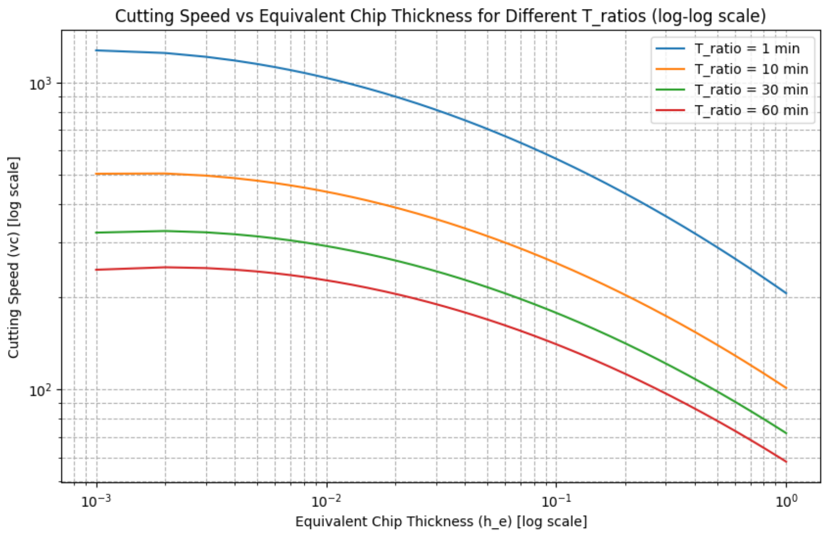

Figure 41: *CGI 450 CC Cutting Speed vs Equivalent Chip Thickness for Different T_ratios.*

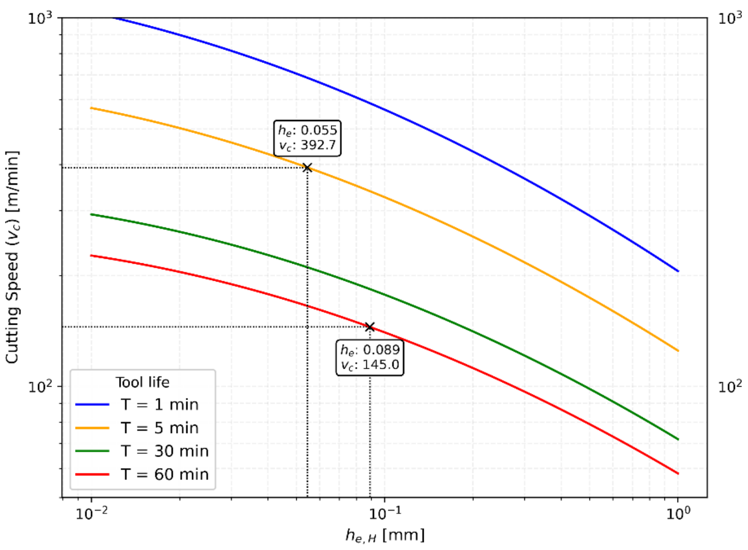

Figure 42: *CGI 450 CC Colding results h_e.*

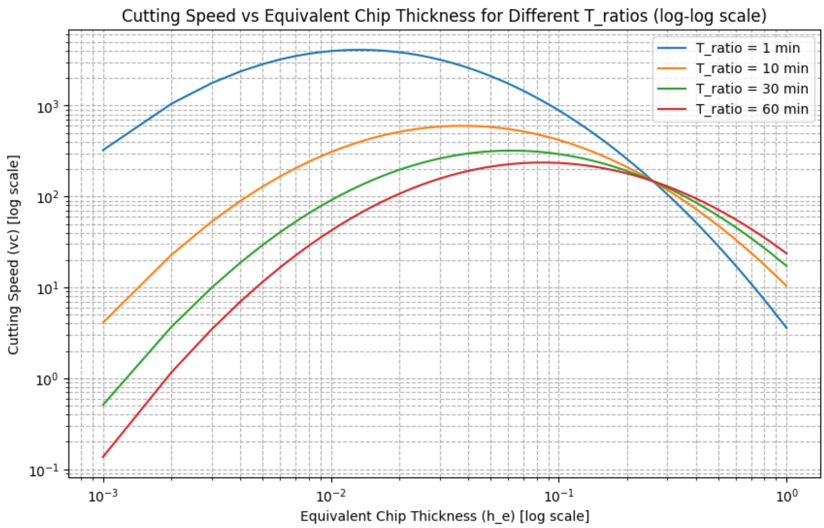

Figure 43: *SSF350 CC Cutting Speed vs Equivalent Chip Thickness for Different T_ratios.*

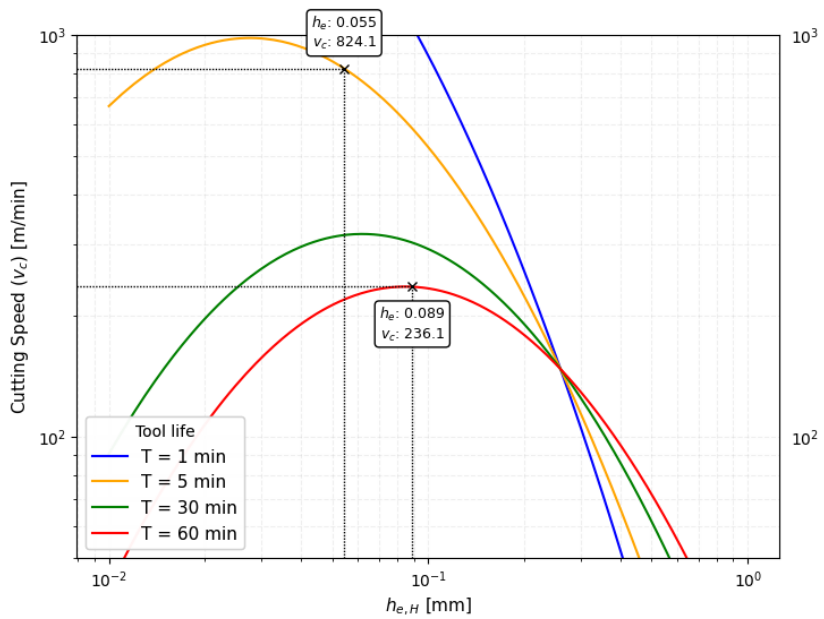

Figure 44: *SSF350 CC Colding results h_e.*

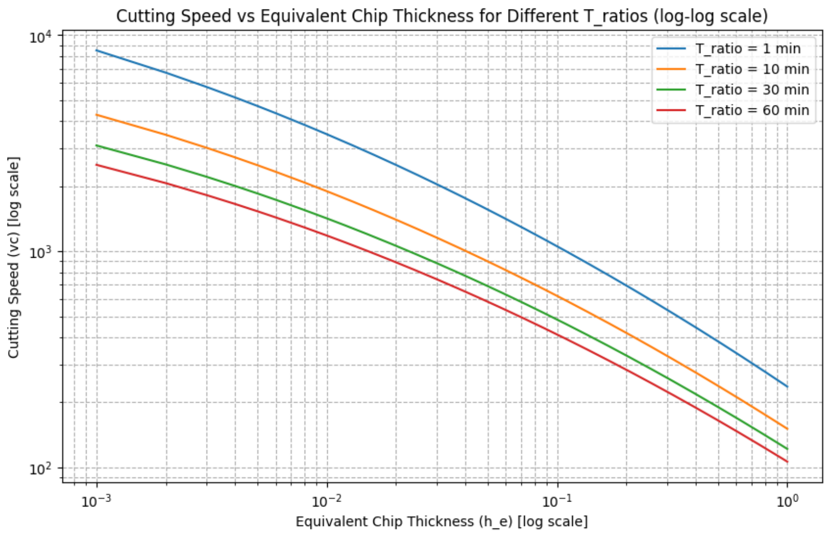

Figure 45: *CGI450 cBN Cutting Speed vs Equivalent Chip Thickness for Different T_ratios.*

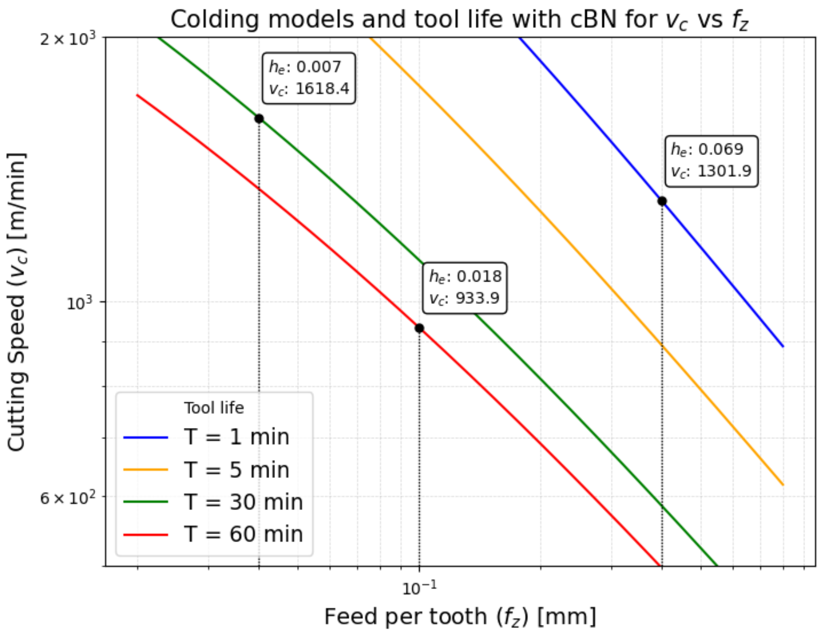

Figure 46: *CGI450 cBN Colding results h_e.*

5. Discussion

As writen in the results, the Colding models for ceramic machining CGI 450 and CC machining SSF 350 exhibit geometric singularities, despite demonstrating good statistical results. To find out this conflict between mathematical accuracy and physical invalidity, it is necessary to examine the fundamental architecture of the Colding equation.

According to Johansson[25], the Colding model is essentially a complex polynomial fitted within a logarithmic domain. While highly effective for capturing steady-state mechanical wear, this mathematical structure is extremely sensitive to non-linear deviations in the empirical data matrix. In certain cases, the experimental tool life does not decrease monotonically with an increased cutting load, which violates the traditional Taylor paradigm. To minimize residual error under these anomalies, the numerical optimization algorithm compensates by driving the empirical constants to extreme values. This mathematical forced-fitting inherently contorts the 3D tool life surface, resulting in unphysical 2D projections characterized by intersecting iso-life curves and inverted slopes.

In the context of this research, the data that triggered these mathematical singularities is not erroneous; rather, it reflects a profound shift in the underlying wear mechanisms. The geometric anomalies observed in these two specific test cases correlate precisely with the conditions under which severe micro-scale chemical reactions were previously identified.

The EDS analysis confirmed the presence of Mg-Si-O deposits on the worn tool surfaces. This finding aligns with the recent study by Bello Bermejo et al.[30]. The deposition of this Mg-Si-O layer explains the anomalies in the Colding model. Standard wear models assume that tool degradation is a monotonic and purely mechanical process. However, the in-situ formation of this Mg-Si-O layer alters the contact conditions at the tool-chip interface. It acts as a transient thermal barrier and solid lubricant. This barrier suppresses the mechanical wear rate at specific high-speed parameters.

When the cutting speed increases, the interface temperature rises. This high temperature accelerates the chemical reaction between Mg, Si, and environmental oxygen. According to Bello Bermejo et al.[30], these deposits may form orthopyroxene structures like $(Mg,Fe)Si_2O_3$ or forsterite Mg_2SiO_4. This chemical interaction disrupts the steady-state wear progression. It creates a non-linear tool life behaviour.

Consequently, the Colding model produces geometric singularities, such as intersecting iso-life curves. These mathematical anomalies are direct evidence of the tribochemical protection layer. The film periodically forms and detaches. This cyclic behaviour violates the assumptions of conventional empirical equations. Therefore, the mathematical singularity represents a physical transition in the wear regime. It proves that the mixed ferritic-pearlitic microstructure of SSF CGI 350 promotes complex interfacial chemistry.

6. Limitations and future work

6.1. Limitations of the study

While this study provides comprehensive insights into the comparative wear behaviour of advanced cutting tools in milling CGI, several methodological and analytical limitations should be noted when evaluating the results.

Firstly, regarding the experimental design, the tool life tests were conducted without statistical repetitions for each parameter set due to practical constraints in material availability and machining time. Consequently, the wear curves and the exact calculated tool life may exhibit sensitivity to stochastic variations inherent in the metal cutting process.

Secondly, early catastrophic failures, such as the initial cBN tool fracture encountered when machining SSF CGI 350, were excluded from the final comparative analysis. This exclusion limits a broader evaluation of severe thermo-mechanical stress mismatches under those specific cutting conditions.

Lastly, the characterization of the protective Mg-Si-O layer relies predominantly on EDS. While EDS effectively maps the elemental distribution and overlapping presence of Mg, Si, and O, it is insufficient for definitive crystallographic identification. The classification of these deposits as a specific thermal barrier and solid lubricant remains an informed hypothesis.

6.2. Future work

Future research should address these limitations by incorporating multi-replicate experimental designs to establish robust statistical confidence intervals for tool life data. To move beyond elemental mapping, advanced crystallographic analyses, such as X-ray Diffraction (XRD) or Transmission Electron Microscopy (TEM), will be crucial for validating the precise phase composition and structural properties of the tribo-layers.

Additionally, future work should investigate the influence of coolant-assisted or minimum quantity lubrication (MQL) machining conditions on the formation and stability of the Mg-Si-O deposits. Since the current study was conducted under dry cutting conditions, the elevated interface temperatures likely promoted deposits reactions at the tool-chip interface. Introducing lubrication or cooling may alter the thermal and chemical environment, potentially changing both the wear mechanisms and the stability of the empirical Colding model predictions.

7. Conclusion

This thesis investigated the wear mechanisms of advanced cutting tools. The tools milled two distinct compacted graphite iron grades. These were fully pearlitic CGI 450 and ferritic-pearlitic SSF CGI 350. The research linked microscopic chemistry with macroscopic mathematical models. The results show that the matrix composition effects the wear mechanism. CGI 450 has higher hardness. It mainly caused severe abrasive flank wear and comb cracking. In contrast, SSF CGI 350 has a higher ferrite fraction. This made the material much softer and more ductile. As a result, the dominant wear shifted to severe adhesive wear. This included continuous plastic deformation and the frequent formation of BUE.

The study also confirmed the dynamic formation of protective layers. The EDS results found a Mg-Si-O layer. This protection layer formed under extreme thermo-mechanical loads. It acted as a thermal barrier and a solid lubricant. This temporarily reduced wear and extended tool life.

To model these effects macroscopically, Python optimization extracted the Colding tool life constants. The mathematical fit was highly accurate. The prediction errors were consistently below 9%.

However, the Colding model results showed mathematical singularities. These anomalies appeared on ceramic cutting CGI 450 and CC cutting SSF 350. These singularities were not algorithmic errors. They were macroscopic mathematical proofs of the micro-scale chemical interference. The protection layer disrupted normal mechanical wear patterns. This proves that standard empirical models become physically unstable under strong chemical interactions.

In conclusion, optimal machining of advanced cast irons requires a dual approach. Tool selection need to be aligned with the workpiece microstructure. For the highly ferritic SSF CGI 350, CC tools demonstrated the best overall performance. The CC inserts successfully leveraged the dynamic Mg-Si-O tribo-film to mitigate adhesive wear. Conversely, for the harder, fully pearlitic CGI 450, cBN tools proved superior. The cBN substrate effectively resisted the abrasive wear generated by the strong pearlitic matrix. Additionally, defining the absolute optimal condition requires balancing productivity against tool economy. If the primary industrial goal is maximizing the material removal rate, cBN and ceramic tools machining CGI 450 at elevated speeds provide the fastest production cycle. Similarly, for SSF CGI 350, running CC tools at higher speeds maximizes the production output. In contrast, if the manufacturing priority is extending tool life and minimizing costly tool changes, conservative cutting parameters must be applied. For CGI 450, reducing the cutting speed minimizes abrasive wear on the cBN inserts. Machining SSF 350 with CC tools at lower speeds ensures a higher stable wear progression. Ultimately, the best machining strategy depends on the specific economic priorities of the production system.

References

[1] Sirtuli, L. J., Bello Bermejo, J. M., Windmark, C., Norgren, S., Ståhl, J., & Boing, D. (2024). Machining of Compacted Graphite Iron. Journal of Materials Processing Technology, 332, 1-28. https://doi.org/10.1016/j.jmatprotec.2024.118553

[2] Lee, W. J., Wu, H., Yun, H., Kim, H., Jun, M. B., & Sutherland, J. W. (2019). Predictive Maintenance of Machine Tool Systems Using Artificial Intelligence Techniques Applied to Machine Condition Data. Procedia CIRP, 80, 506. https://doi.org/10.1016/j.procir.2018.12.019

[3] Bello Bermejo, J. M., Saatçi, B., Johansson, D., Hägglund, S., Ståhl, J., & Windmark, C. (2025). Optimal modelling of Colding parameters for round inserts with respect to tool use-time criteria. Procedia CIRP, 133, 286. https://doi.org/10.1016/j.procir.2025.02.050

[4] Taylor, F. W. (1907). On the art of cutting metals. American Society of Mechanical Engineers.

[5] Hägglund, S. (2013). Methods and models for cutting data optimization. Chalmers University of Technology.

[6] Saatçi, B. (2024). Tool life prediction of cemented carbide tools during milling of compacted graphite iron [Master's thesis, Lund University]. LUP Student Papers. https://lup.lub.lu.se/student-papers/record/9151270

[7] Ståhl, J.-E.(2012) Metal cutting theories and models, Seco Tools AB.

[8] Kihlberg, E., Norman, V., Skoglund, P., Schmidt, P., & Moverare, J. (2021). On the Correlation Between Microstructural Parameters and the Thermo-Mechanical Fatigue Performance of Cast Iron. International Journal of Fatigue, 145, . https://doi.org/10.1016/j.ijfatigue.2020.106112

[9] Ruggieri, C. (2024). A probabilistic model to predict specimen geometry effects on fracture toughness in ferritic–pearlitic steels. *Engineering Fracture Mechanics*, *310*, . https://doi.org/10.1016/j.engfracmech.2024.110493

[10] Flom, D., Reed, W., Jr., Hibbs, L., Jr., & Broskea, T. (1991). High-speed machining of cast iron with BZN compacts. Wear, 147(2), 253-265. https://doi.org/10.1016/0043-1648(91)90183-U

[11] Johansson, D., Lindvall, R., Fröström, M., Bushlya, V., & Ståhl, J. (2018). Equivalent Chip Thickness and its Influence on Tool Life. *Procedia Manufacturing*, *25*, 344. https://doi.org/10.1016/j.promfg.2018.06.102

[12] G.S, U. (2004). Trent E.M., Wright P.K. *Science of Sintering*, *36*(1), 54. https://doi.org/10.2298/SOS0401054U

[13] Fiorini, P., & Byrne, G. (2016). The influence of built-up layer formation on cutting performance of GG25 grey cast iron. CIRP Annals - Manufacturing Technology, 65(1), 93-96. https://doi.org/10.1016/j.cirp.2016.04.045

[14] Tomala, A., Ripoll, M. R., & Badisch, E. (2013). Tool – Solid Lubricant – Workpiece Interactions in High Temperatures Applications. *Procedia Engineering*, *68*, 626. https://doi.org/10.1016/j.proeng.2013.12.231

[15] Sandvik Coromant. (n.d.). R200-068Q27-12M. Available: https://www.sandvik.coromant.com/en-us/product-details?c=r200-068q27-12m

[16] Sandvik Coromant. (n.d.). RCKT 12 04 MO 6190. Available: https://www.sandvik.coromant.com/en-gb/product-details?m=5740451

[17] Sandvik Coromant. (n.d.). A1B05-40 27 035. Available: https://www.sandvik.coromant.com/en-gb/product-details?c=A1B05-4027035

[18] Seco Tools. (n.d.). R220.29I-0080-06.6A. Available: https://www.secotools.com/article/p_02949625

[19] Seco Tools. (n.d.). RPKW1204M0T6-MD10, MK2050. Available: https://www.secotools.com/article/p_02923731?pf=true&entryPoint=ProductTree

[20] Seco Tools. (n.d.). R220.70-0063-09-6. Available: https://www.secotools.com/article/p_00023749

[21] Seco Tools. (n.d.). RNMN120300S CBN300. Available: https://www.secotools.com/article/p_00097855

[22] Seco Tools. (n.d.). DIN40ADB-SM22-035-L1. Available: https://www.secotools.com/article/p_10007164

[23] Evident Scientific. (n.d.). Olympus SZX7. Available: https://evidentscientific.com/en/products/upright/szx7

[24] Struers, n.d. Cast iron: Metallographic preparation, Struers Knowledge. Available: https://www.struers.com/en/knowledge/materials/cast-iron#preparationmethod

[25] Johansson, D. (2019). Tool Life and Cutting Data Modelling in Metal Cutting. Mechanical Engineering, Faculty of Engineering, Lund University. https://portal.research.lu.se/en/publications/tool-life-and-cutting-data-modelling-in-metal-cutting-testing-mod/

[26] Khadka, S., Rahman Rashid, R. A., Navarro-Devia, J. H., Papageorgiou, A., Stephens, G., Hägglund, S., & Palanisamy, S. (2025). A Comparative Study of Mathematical Methods for Determining Colding's Constants for Milling of Steels and Experimental Validation. Journal of Manufacturing and Materials Processing, 9(6), 189. https://doi.org/10.3390/jmmp9060189

[27] Lindvall, R. (2024). Wear mechanisms in cutting tools for machining applications. Lund University, Faculty of Engineering, Department of Mechanical Engineering Sciences, Division of Production and Materials Engineering. https://portal.research.lu.se/en/publications/wear-mechanisms-in-cutting-tools-for-machining-applications-inter/

[28] Zhu, L., Evans, R., Zhou, Y. and Ren, F. (2022) 'Wear Study of Cubic Boron Nitride (cBN) Cutting Tool for Machining of Compacted Graphite Iron (CGI) with Different Metalworking Fluids', Lubricants, 10(4), p. 51. Available: https://doi.org/10.3390/lubricants10040051.

[29] Zhu, Q. (Ed.). (2024). Ceramic films and coatings: Properties and applications. MDPI. https://doi.org/10.3390/books978-3-7258-1028-4

[30] Bello Bermejo, J. M., Lindvall, R., Saatçi, B., Ståhl, J., Åberg, L. M., Bohlin, O., & Windmark, C. (2025). Wear behaviour of PVD (Ti,Si)N-(Ti,Al)N coated cemented carbide in down milling pearlitic compacted graphite iron. Wear, 570, . https://doi.org/10.1016/j.wear.2025.205891

Appendix A: Tool life data

Table 2: *CGI450 Ceramic*

fz(mm/rev)	vc(m/min)	passes	MRR (mm^3/min)	Total volume (mm^3)
0.271	732	47.39	31571.88437	473900
0.1	900	106.38	14323.94488	1063800
0.42	600	49.27	40107.04566	492700
0.42	490	66	32754.08729	660000
0.271	490	60	21134.18489	600000
0.15	650	57	15517.60695	570000
0.1	1050	180	16711.26902	1800000
0.1	1200	130	19098.59317	1300000

Table 3: *CGI450 CC*

fz(mm/rev)	vc(m/min)	passes	MRR (mm^3/min)	Total volume (mm^3)
0.4	250	67.53	15.91549431	675.3
0.554	154	218.079	13.57846312	2180.79
0.277	431	27.74	19.00103119	277.4
0.277	185	138.3	8.155895059	1383
0.554	359	62	31.65369001	620
0.554	250	72	22.04295962	720
0.4	393	32	25.01915705	320
0.477	317	48	24.06565979	480

__Table 4:__ CGI450 cBN

fz(mm/rev)	vc(m/min)	passes	MRR (mm^3/min)	Total volume(mm^3)
0.15	1000	127.4	7957.747155	
0.1	1300	204	41380.2852	1848750
0.05	1500	198	11936.62073	1794375
0.05	1000	288	7957.747155	2610000
0.2	1300	72	41380.2852	652500
0.1	1600	72	25464.79089	652500
0.15	1500	72	35809.8622	652500
0.07	1700	71	18939.43823	643437.5

__Table 5:__ SSF CGI350 Ceramic

fz(mm/rev)	vc(m/min)	passes	MRR (mm^3/min)	Total volume (mm^3)
0.271	996	36.02353	42.95846562	360.2353
0.1	1200	8.192758	19.09859317	81.92758
0.1	810	16.40219	12.89155039	164.0219
0.271	450	37.6184	19.40894531	376.184
0.15	550	42.92682	13.13028281	429.2682
0.1	400	42.56654	6.366197724	425.6654
0.42	400	92.15371	26.73803044	921.5371
0.42	500	89.53548	33.42253805	895.3548
0.37	600	56.60116	35.33239737	566.0116
0.271	550	35.7456	23.72204427	357.456

Table 6: *SSF CGI350 CC*

fz(mm/rev)	vc(m/min)	passes	MRR (mm^3/min)	Total volume (mm^3)
0.477	295	269.164	22.39548782	2691.64
0.277	480	104.4115	21.16124123	1044.115
0.554	480	100.7209	42.32248247	1007.209
0.554	234	430.8597	20.6322102	4308.597
0.277	375	124.8662	16.53221971	1248.662
0.5	450	125.1699	35.8098622	1251.699
0.525	515	101.0481	43.03151774	1010.481
0.477	375	160.6055	28.46884045	1606.055

Table 7: *SSF CGI350 cBN*

fz(mm/rev)	vc(m/min)	passes	MRR (mm^3/min)	Total volume (mm^3)
0.07	700	28.04549	7.798592212	280.4549
0.15	500	20.94073	11.93662073	209.4073
0.07	1700	4.245697	18.93943823	42.45697
0.07	2000	7.893462	22.28169203	78.93462
0.07	2200	7.120289	24.50986124	71.20289
0.15	2000	9.308867	47.74648293	93.08867
0.2	2000	13.33861	63.66197724	133.3861

Appendix B: Microscopy

Due to the extensive volume of collected microscopy data, this appendix presents a targeted selection of images. It focuses exclusively on the 2 tool-workpiece combinations that produced mathematical singularities during the Colding modelling. These combinations are CC machining SSF CGI 350 and ceramic machining CGI 450. For each of these 2 cases, the included images represent the specific cutting test that achieved the best overall tool performance.

Table 8: *Microscopy of SSF CGI350 CC*

Pass 018	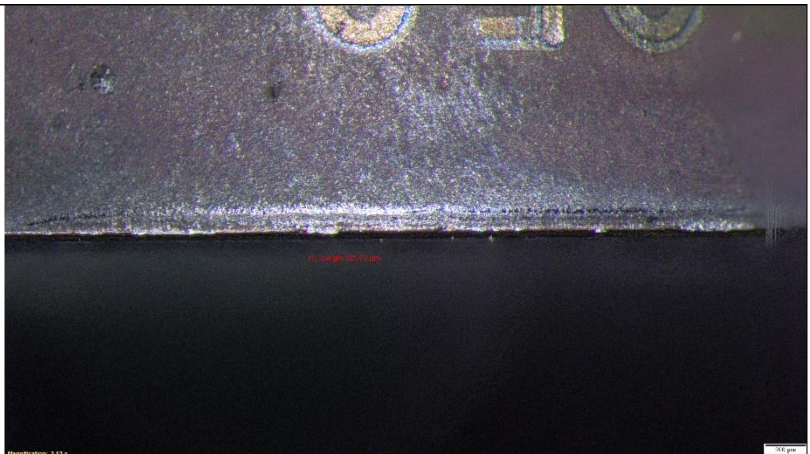
Pass 036	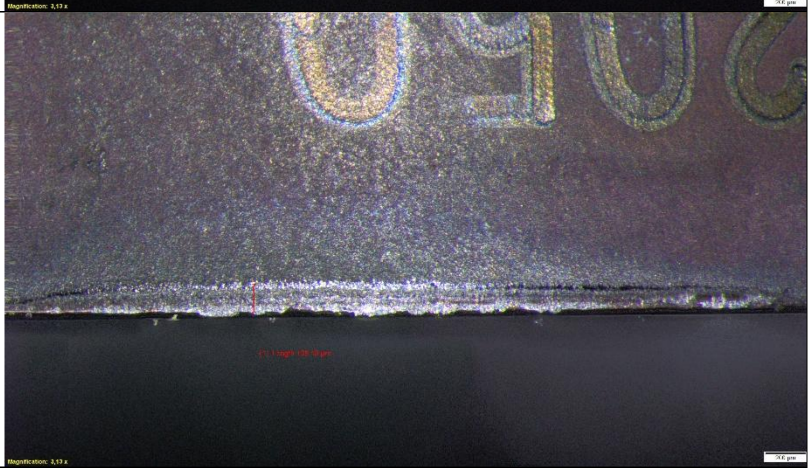

Pass 054	
Pass 072	
Pass 090	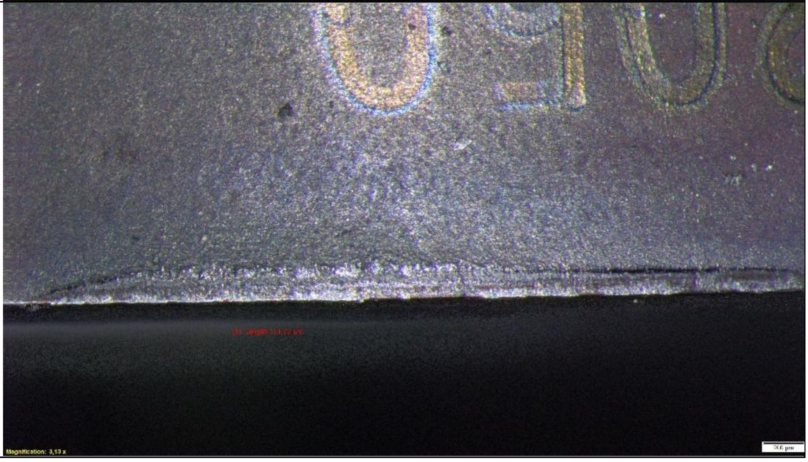

Pass 108	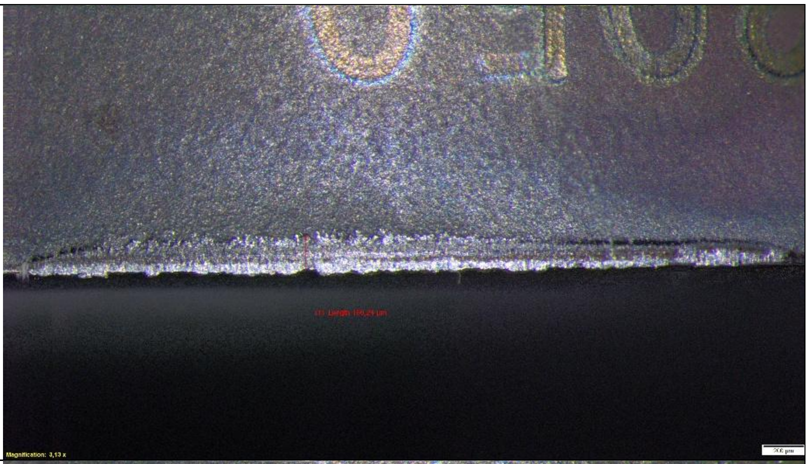
Pass 126	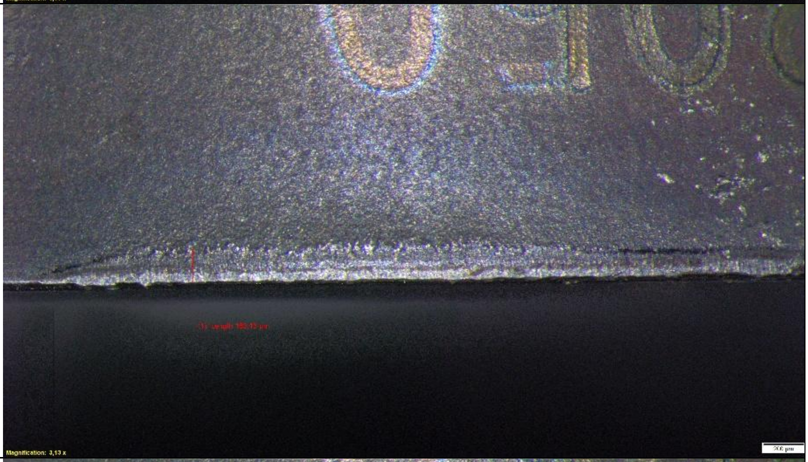
Pass 144	

Pass 162	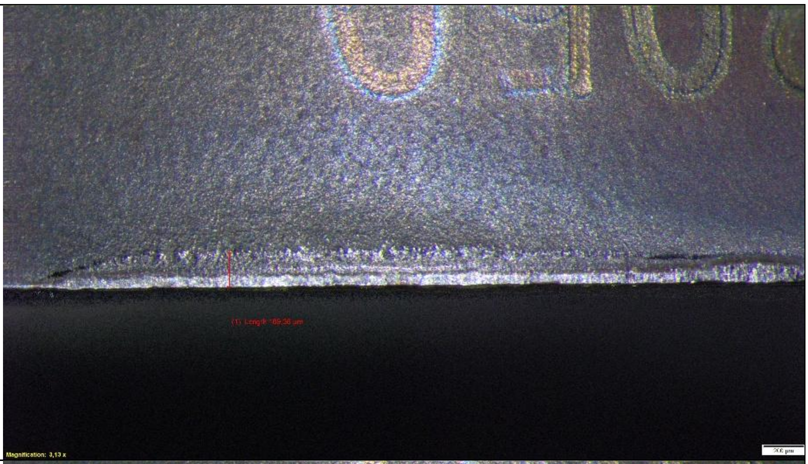
Pass 168	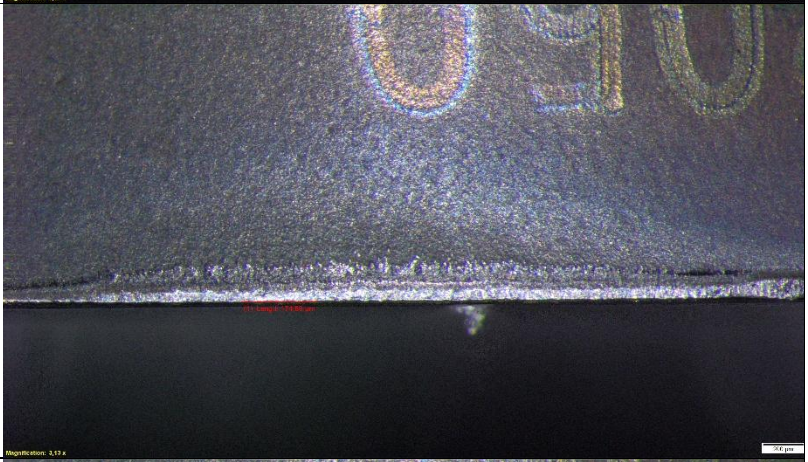
Pass 198	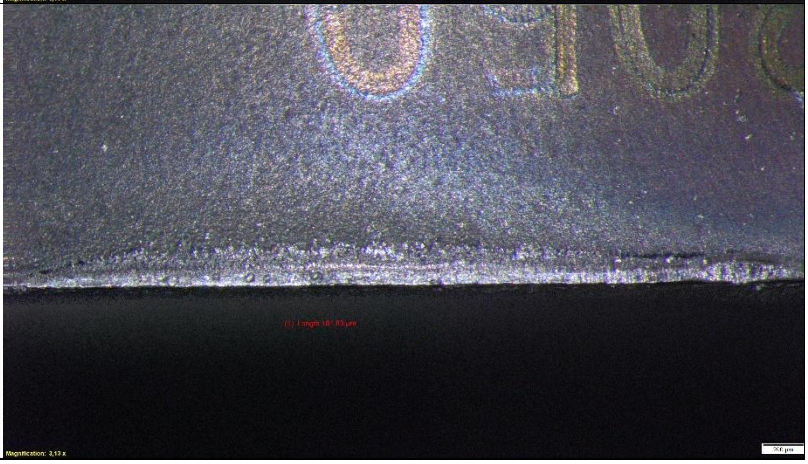

Pass 234	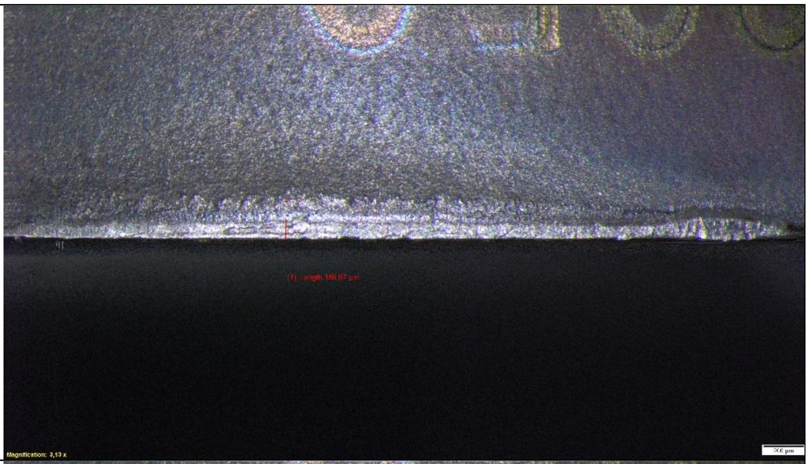
Pass 270	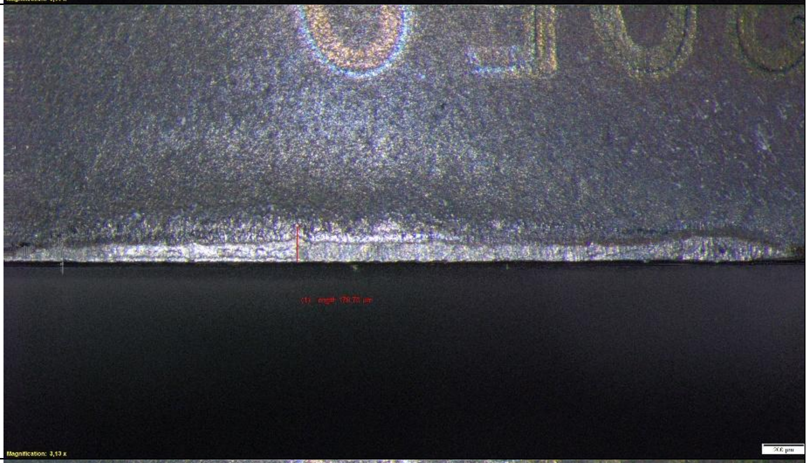
Pass 324	

Pas s 378	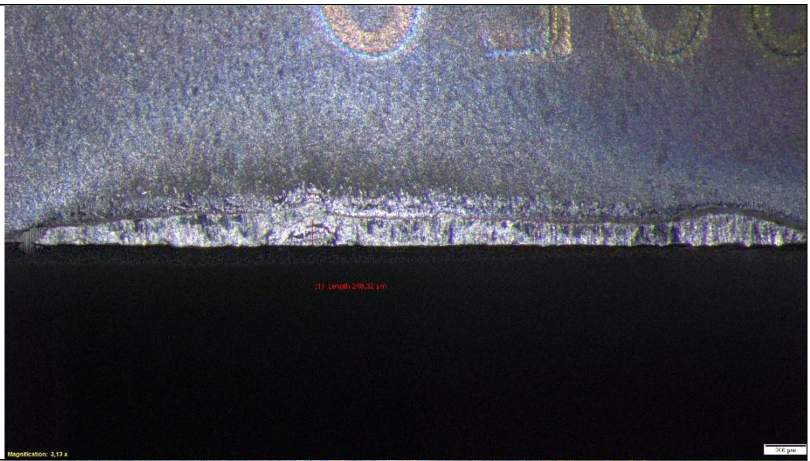
Pas s 396	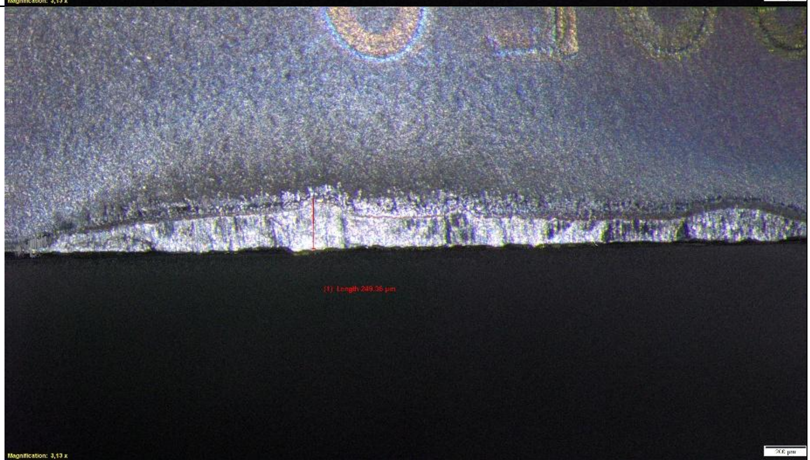
Pas s 414	

Pass 420		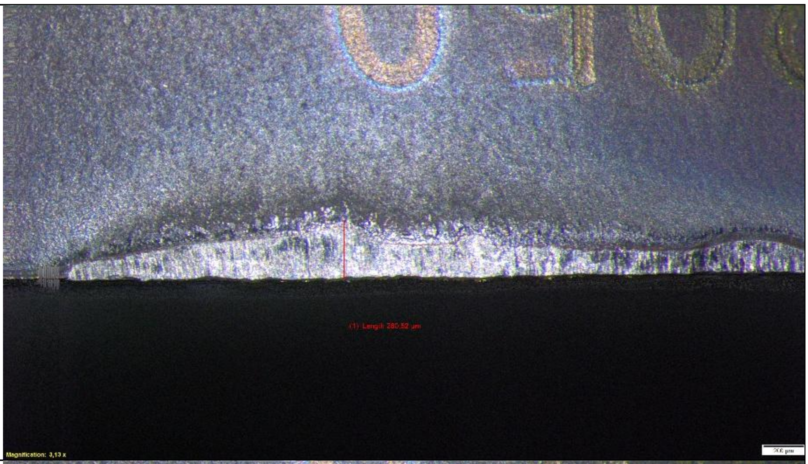
Pass 426		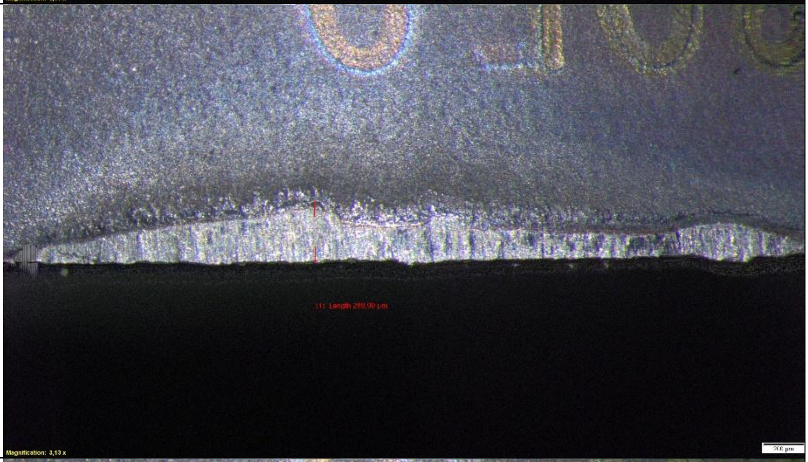
Pass 432		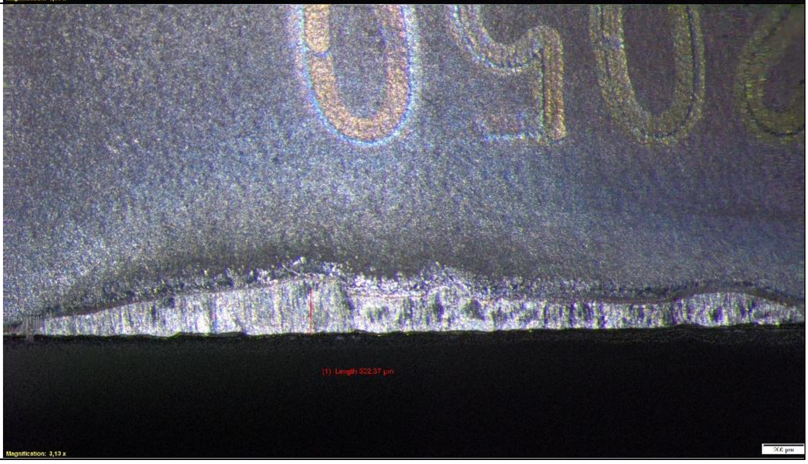

__Table 9:__ Microscopy of CGI450 ceramic under fz=0.1 and vc=1050

Pass 001	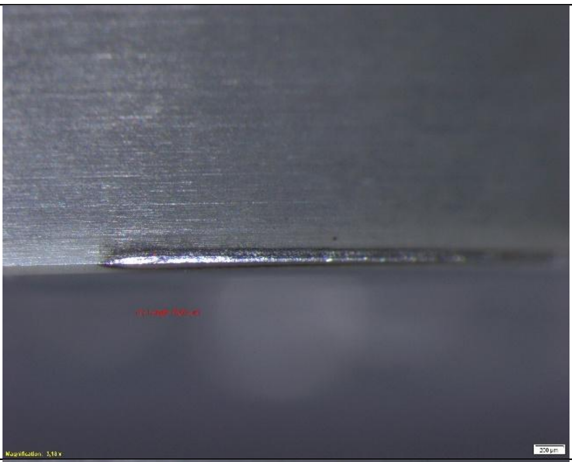
Pass 006	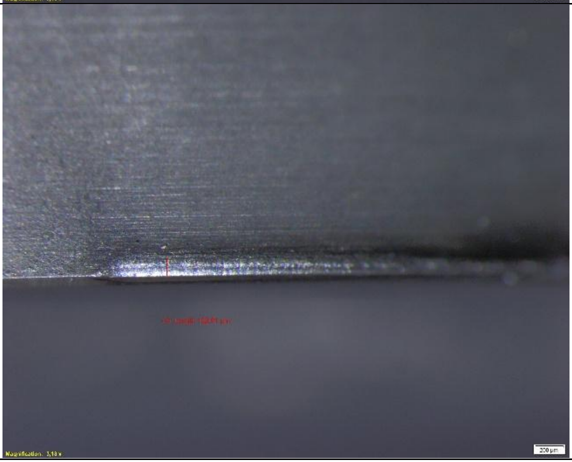

Pass 012	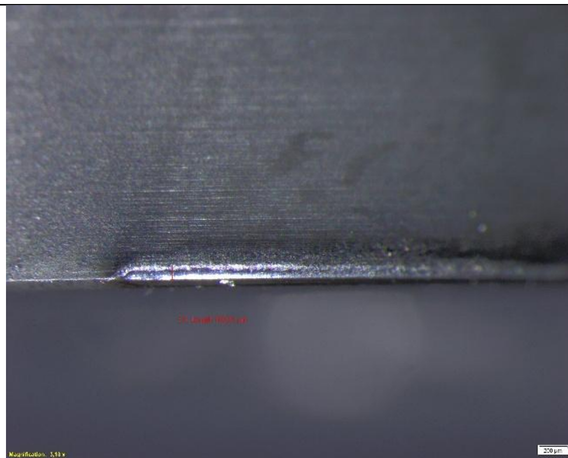
Pass 018	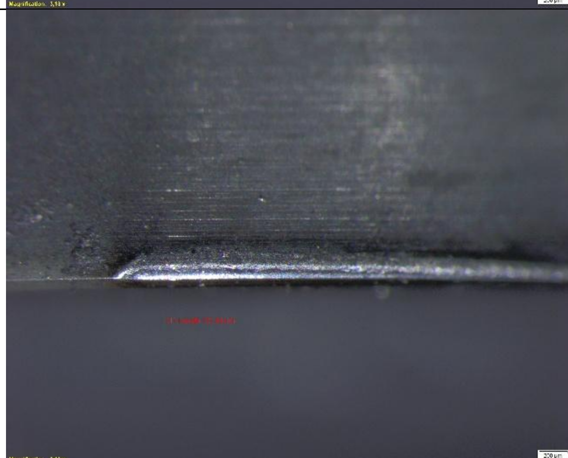
Pass 024	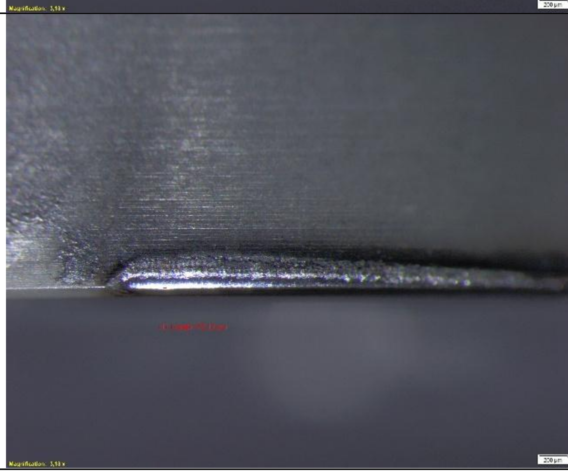

Pass 030	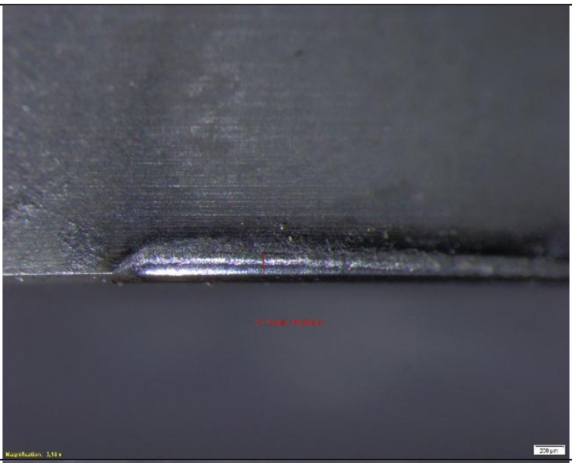
Pass 036	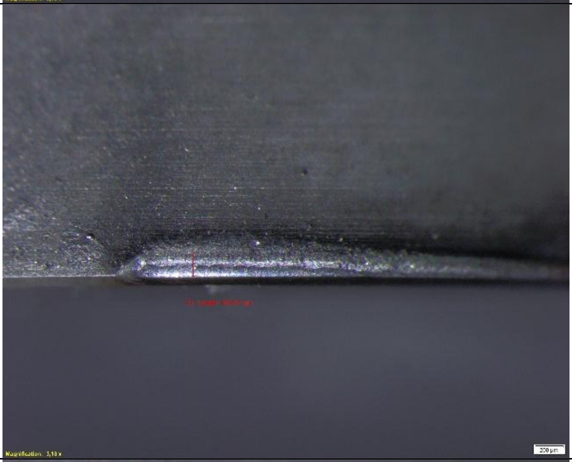
Pass 042	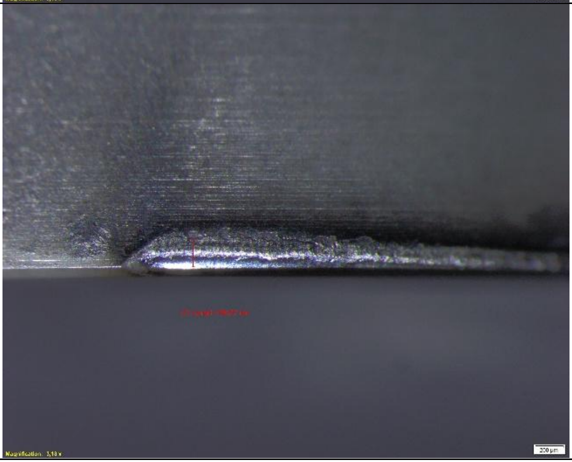

Pass 048	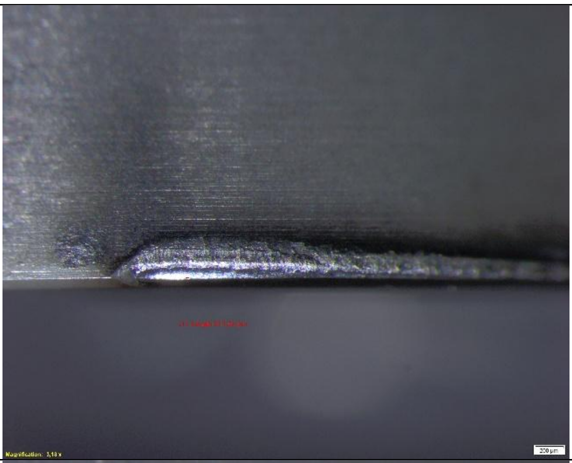
Pass 054	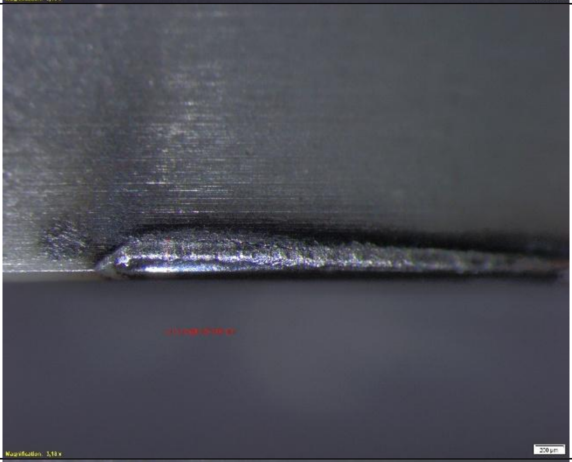
Pass 060	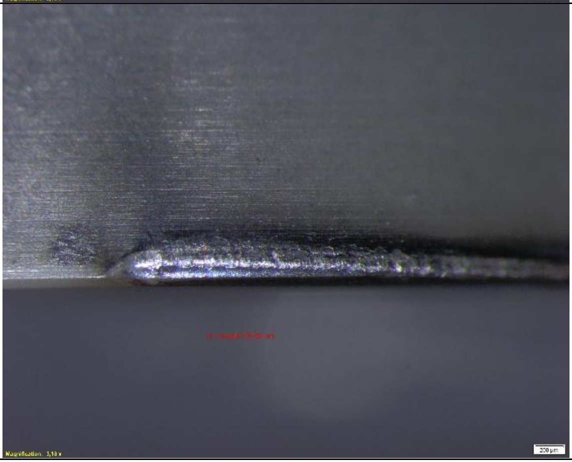

Pass 066	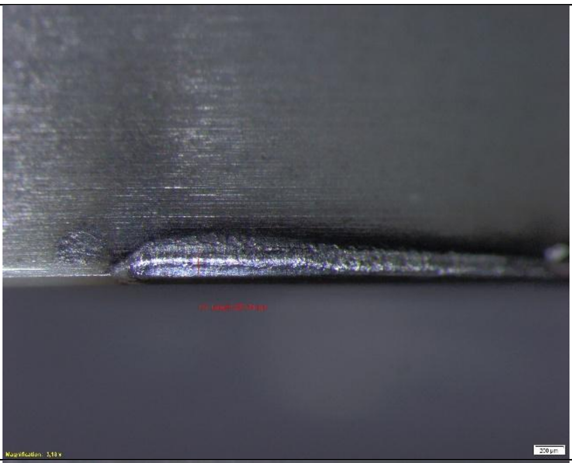
Pass 072	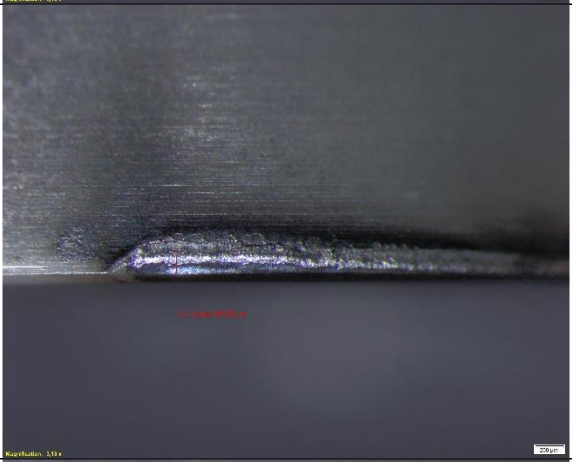
Pass 078	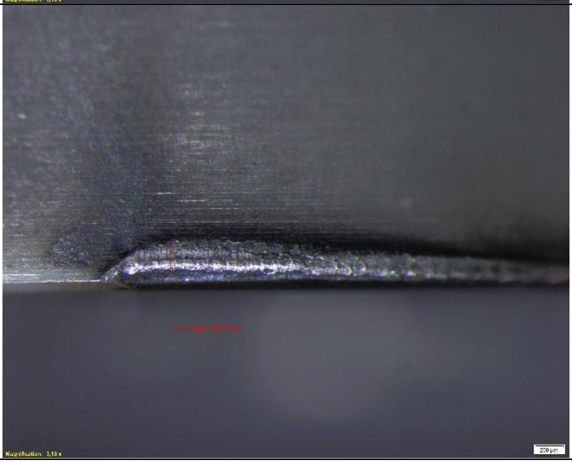

Pass 084	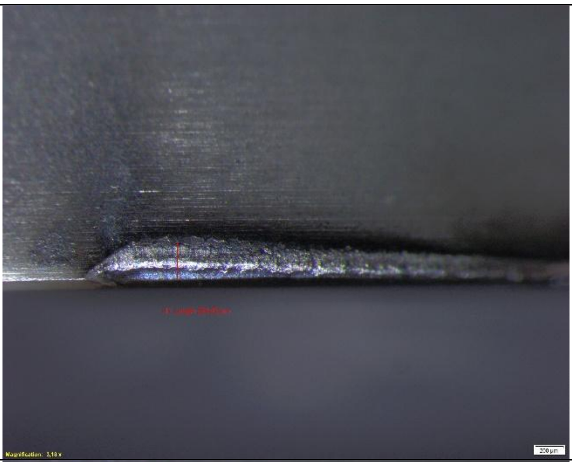
Pass 090	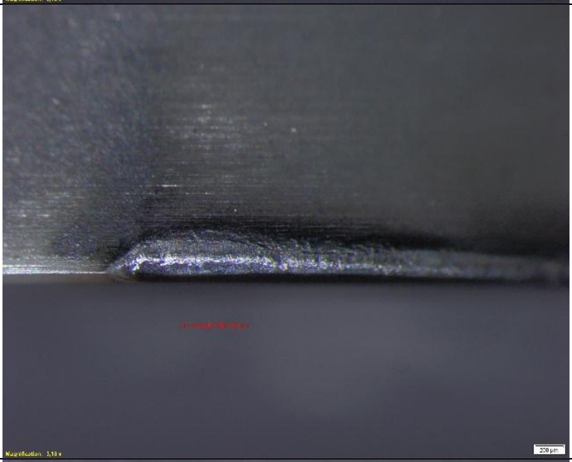
Pass 096	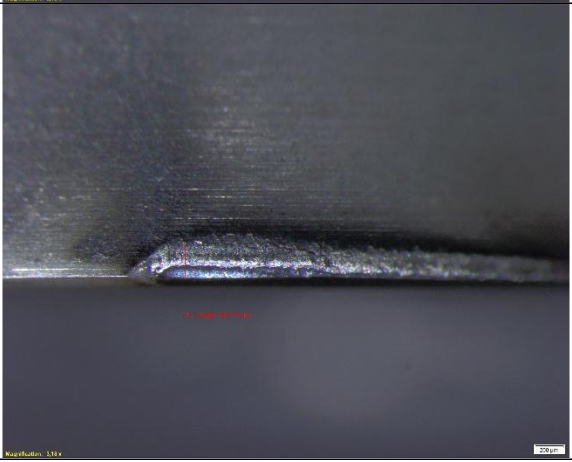

Pass 102	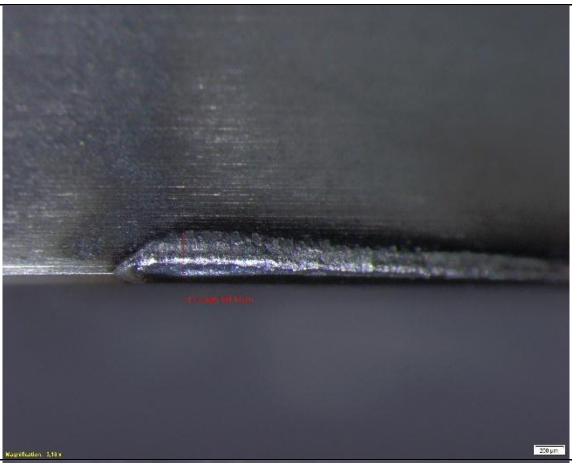
Pass 108	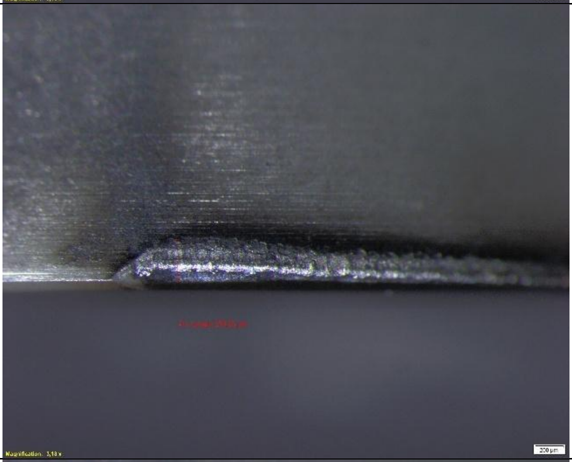
Pass 114	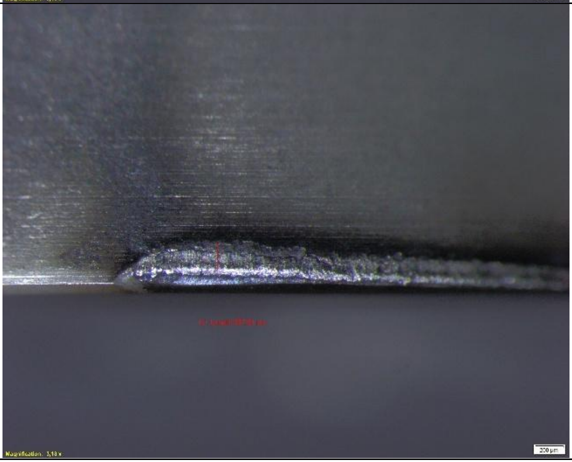

Pass 120		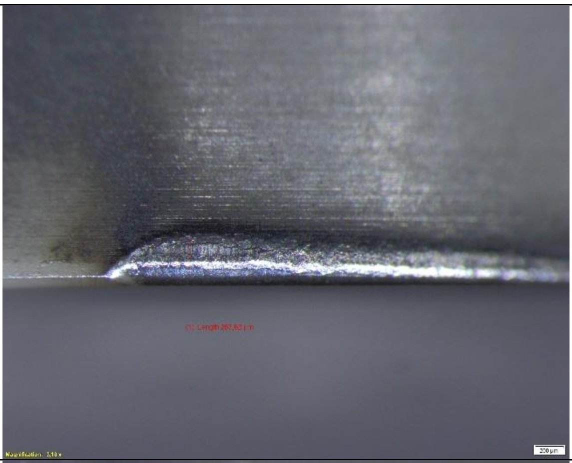
Pass 126		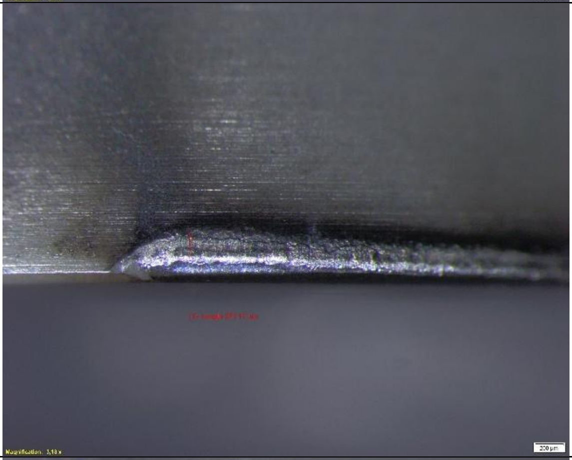
Pass 132		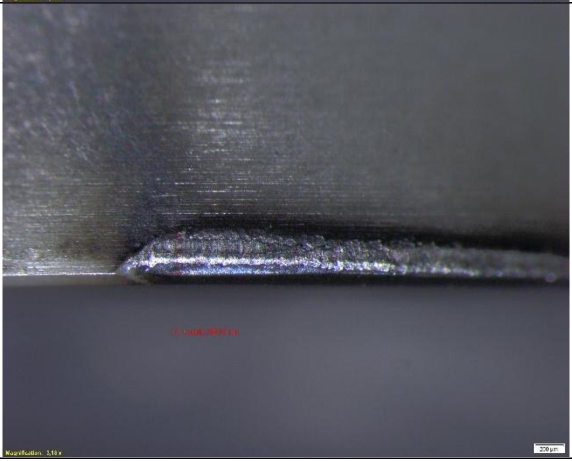

Pass 138		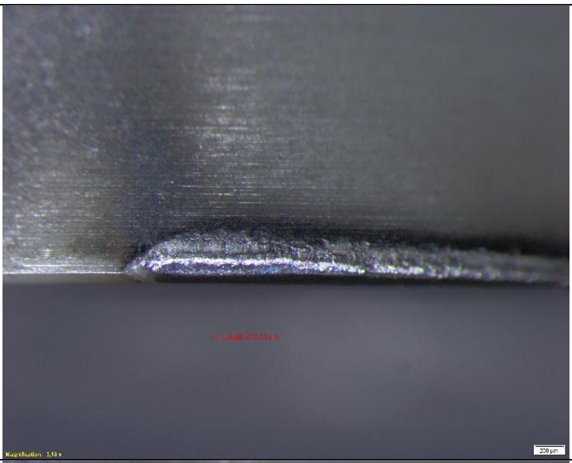
Pass 144		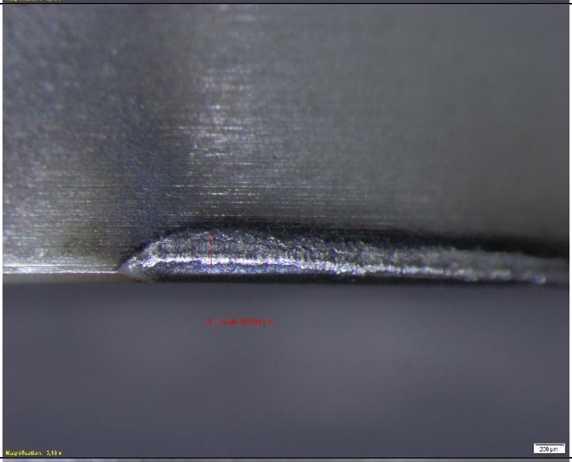
Pass 150		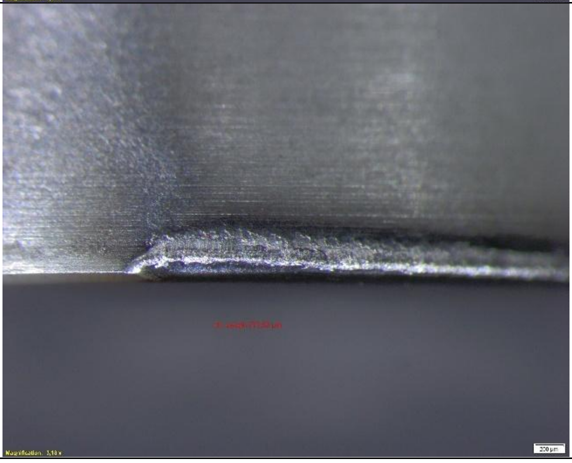

Pass 156	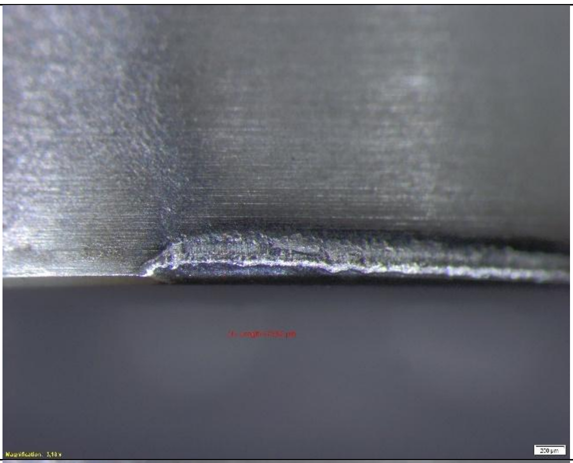
Pass 162	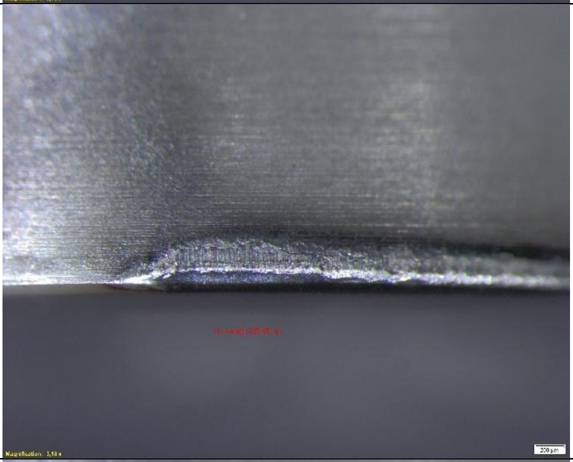
Pass 168	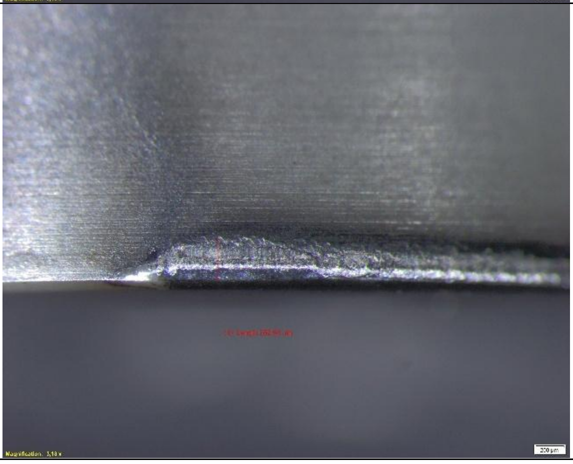

Pass 174	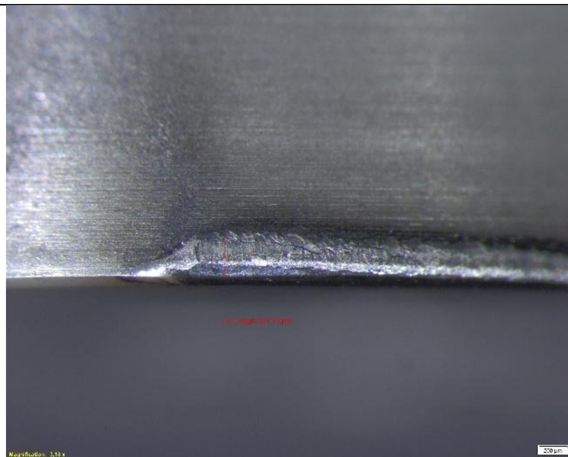
Pass 180